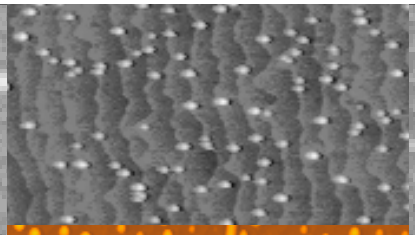

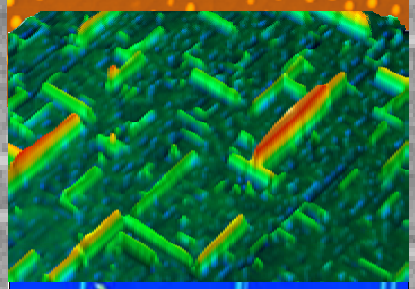

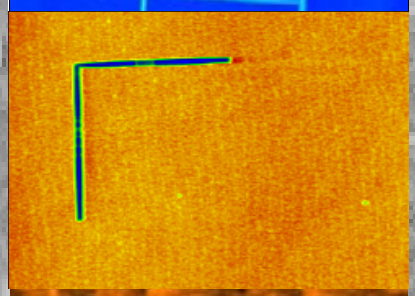

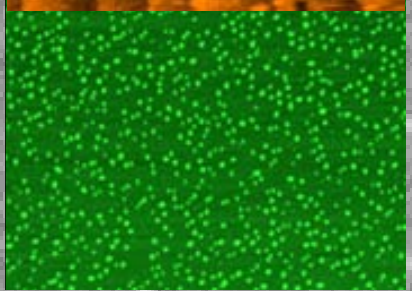
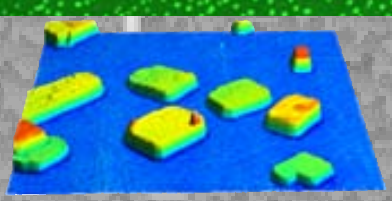
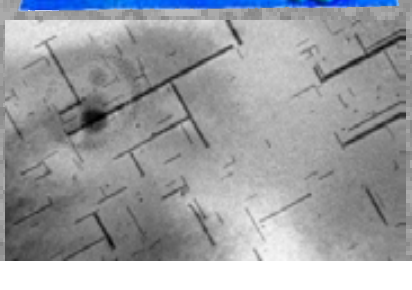

Self-assembled strain-induced oxide nanostructures grown by chemical solutions

Marta Gibert Gutiérrez

PROGRAMA DE DOCTORAT EN CIÈNCIA DE MATERIALS
Departament de Física de la Universitat Autònoma de Barcelona

Departament de Materials Superconductors i Nanoestructuració a Gran Escala ICMAB-CSIC

Directors: Prof. Xavier Obradors
Dra. Teresa Puig

Tutor: Dr. Javier Rodríguez-Viejo

Bellaterra, 14 de gener del 2009

Self-assembled strain-induced oxide nanostructures grown by chemical solutions

Marta Gibert Gutiérrez

PROGRAMA DE DOCTORAT EN CIÈNCIA DE MATERIALS
Departament de Física de la Universitat Autònoma de Barcelona

Departament de Materials Superconductors i Nanoestructuració a Gran Escala
ICMAB-CSIC

Directors: Prof. Xavier Obradors i Dra. Teresa Puig

Tutor: Dr. Javier Rodríguez-Viejo

Memoria presentada per a l'obtenció del grau de doctor

Bellaterra, gener 2009

"Crystal growth is a science and an art"
Margaret (Peggy) C. Etter

Acknowledgments

With these words I would like to thank all the people who have made possible this work through their help, knowledge and friendship, particularly:

First of all, I would really like to acknowledge my supervisors, Prof. Xavier Obradors and Dra. Teresa Puig, for their confidence in me, their helpful advises, for all the opportunities they have given to me, and for all the time, discussions and chats we have sheared.

To all the Superconducting Materials and Nanostructuration Department of ICMAB, specially the staff members, technicians, previous PhD students and post-docs who supported and gave me the adequate background and complementary knowledge for the research developed in this thesis, from the solution based synthesis to the growth of CSD thin films, characterization and analysis of functional properties.

To. P. Abellán, Dr. A. Benedetti and Dr. F. Sandiumenge for all the TEM work they have provided, which have become essential for the comprehension and study of interfacial nanoislands. I address a special thanks to P. Abellán, for her enthusiasm and ability preparing TEM samples, and last TEM corrections.

To Dr. J. Gutiérrez and Dra. A. Palau for the PPMS measurements and corresponding analyses, and for their help. I also thank Dra. A. Palau for the ion milling experiments based in FIB carried out in the IMB-CNM facilities. Thanks to the support of those facilities that make possible this experiment.

To Dr. A García from Materials Simulation and Theory Department of ICMAB for all the time devoted and contributions from his theoretical point of view to extended discussions on interfacial nanoislands' formation and evolution.

To the group of Dr. B. Holzapfel in IFW-Dreden, specially to Dr. R. Hühne for the RHEED measurements and for all the time he dedicated to me when I was in the IFW-Dresden.

To Dr. J. Martín Gago and his group in ICMM-CSIC for the XPS measurements.

To N. Romà who taught me most of the things when I arrived at ICMAB, and for her continuous support in "Sibèria".

To. P. Álvarez for all the secretary work, attention and efficiency.

To Dr. L. Civale and B. Maiorov for the nice time I spent in Los Alamos National Laboratory (New Mexico-USA), and for their encouragement, helpfulness and rich discussions.

Particular thanks must be given to all those who provided indispensable technical assistance at ICMAB scientific-technical services. To Dr. A. Pérez and M. Simón for their teaching and support with AFM, and patience while I broke tips. To A. Crespi "GADDS" for her motivation and efficiency performing XRD² measurements and the time devoted to develop specific routines for the characterization of the nanoislands. To. J. M. Pérez "Serranito" and B. Bozzo for SQUID measurements, and to A. Carrillo for the SEM and FESEM images. To J. Rubio and M. Lopez for their help to print this manuscript.

To "Ministrio de Educación y Ciencia" for FPU fellowship. To EU projects HIPERCHEM, SUPER3C, NESPA, to the Spanish Ministery (CONSOLIDER NANOSELECT, NANOARTIS, NANOFUNCIONA), to CSIC (CANAMUS) and Generalitat de Catalunya (XARMAE, Pla de Recerca) for financial support.

I would really like to thank all colleagues and friends, past and present, of my group that have made my work at ICMAB so enjoyable.

Especialment, m'agradaria agraïr a la Neus+ per la seva confiança i les moltíssimes estones i converses compartides. Als meus companys i amics de despatx, l'Anna P. Amb qui vaig compartir la taula els primers temps, al Joffre i els seus *Karparinoff's* Δ, i a l'Anna LL. per fer tan agradable el despatx aquests darrers dies de tesis. Al Roberto, pel seu suport i ànims per fer-me *laburar*. A la Patricia Al. per les moltes "cosetes" compartides i totes les rialles i resums. Al César i la Jone, el meu "equip AFM", per la seva amistat i confiança però sobretot pel seu suport incondicional davant l'AFM. A la Patricia Ab., Roxana, la Katerina, el Carlos, la Stef, l'Awa, la Marta,... i a tots aquells que fan i han fet els dies a l'ICMAB agradables, engrescadors i motivants.

No pot faltar un agraïment molt especial i sincer a tota la meva família i, sobretot, als meus pares, Pere i Anna, i al meu germà, Ferran, pel seu suport incondicional en tot moment, disponibilitat total i per la gran estima que els tinc.

Finalment, vull donar les gràcies a l'Aleix per estar en tot moment al meu costat.

To all them, to all of you, thank you very much!!
A tots ells, a tots vosaltres, moltíssimes gràcies!!!

Table of contents

Motivation

The appearance of new functionalities and devices based on shape- and size-dependent properties has triggered in the last decades an enormous interest in creating well-defined structures at nanometric scale. In this framework, self-assembling and self-organizing processes arise as a very general bottom-up approach for the generation of uniform nanostructures with narrow size distributions and high tendency to form ordered arrays. Particularly, self-assembling principles taking advantage of strains associated to heteroepitaxial growth are an attractive fabrication route which has been intensively investigated in the semiconductor field. In this area, its capabilities to generate innovative electronic and optoelectronic devices based on quantum effects have already been widely proved through the generation of structures like nanodots or nanowires. Self-assembling and self-organizing mechanisms are also showing their potential in other expanding disciplines such as the arrangement of metals or molecules. Nevertheless, their application in oxide materials has been scarcely investigated till the moment. Even though, these processes are also considered promising and efficient strategies for the preparation of new devices with innovative functionalities in fields such as ferromagnetism, ferroelectricity, optics or superconductivity.

Preparation of self-assembled interfacial nanostructures is generally based on physical deposition methodologies requiring of vacuum chambers. However, fabrication and implementation of all up-and-coming nanostructures and nanodevices must strongly consider its viability in terms of economic costs and large-scale applicability. In this context, and despite hardly applied up to now, Chemical Solution Deposition (CSD) is a very appealing low-cost approach for the generation of interfacial oxide nanostructures, bearing a high interest for many functionalities and practical applications when the use of large areas or long lengths is required.

In this thesis, we have considered the generation of templates with interfacial self-assembled strain-induced oxide nanostructures based on the deposition of ultradiluted chemical solutions. Hence, the novelty of the work presented is two-fold since it deals with the emergent

field of oxide interfacial nanostructures and demonstrates the possibility to use chemical solutions to obtain self-assembled epitaxial nanoislands with notable tendency to self-organize. Different oxide phases have been studied proving the validity and generality of CSD for the generation of nanostructured templates. It is showed that the shape, size, density and distribution of the resulting interfacial nanoislands can be finely controlled through growth conditions (atmosphere, temperature, time) and solution's concentration.

Combination of experiments and theoretical analyses is a powerful tool for the comprehension of the systems and even points out the possibility to nanoengineer the templates. The experimental work presented based on detailed investigation into morphology and structure of oxide nanoislands is completed with an extended theoretical study about the thermodynamic stability of the islands and the influence of kinetic phenomena on their evolution. It is of special relevance the generation of extremely long nanowires oriented along well-precise directions through the control of elastic relaxation and surface energies. It is also of interest the generation of templates with self-assembled nanodots spontaneously ordered in rows with the steps of the vicinal single-crystal substrates as consequence of the high interfacial energy between lattice steps and islands.

The oxides investigated in this work serve us as model systems and, thus, the results obtained are of general interest and application. Moreover, some features like the generation of nanowires taking advantage of the misfit anisotropy in the growth of dissimilar crystallographic structures can even extend to other materials. Hence, the methodology presented exhibits a great potential for the generation of a large variety of devices at nanoscale. For example, the case of the cerium oxide system investigated could result into a first generation of ionic conductors. Particularly, we show an application of oxide nanostructured templates in the field of high temperature superconductors. Improvement of vortex pinning capabilities in superconductor thin films constitutes nowadays both a challenging scientific issue and a technological problem to solve in their optimization for commercial use. We use interfacial oxide nanostructures as templates to generate artificial vortex pinning centres in $YBa_2Cu_3O_7$ thin films also prepared from chemical solutions. Significant improvement observed at high temperature and high magnetic fields evidence the potential and interest of this new generation of superconductor films based on the control of interfaces at the nanoscale.

Chapter 1

Introduction

1.1 Nanoscience and nanotechnology; self-assembling and self-organizing processes

The capacity to work and handle structures about half million of times smaller than this comma , for example, has revolutionized the science in the last decades. It is the so called world of nanoscience and nanotechnology. Despite nanoparticles were already used by Romans more than 2000 years ago as pigments to decorate ceramics with bright colours, it has not been till recently that the development of new techniques of synthesis and characterization has made possible the study, control, design and application of nanomaterials.

The prefix *nano*, which in Greek means "dwarf", indicates that we are dealing with materials with dimensions of the order of nanometers (10^{-9} m); objects typically measuring from 1 to 100 nm (although the definition is somewhat arbitrary), in the mesoscopic regime between isolated atoms or molecules and bulk material. A human hair is about eighty thousand nanometers width; the nail of our little finger measures ten million nanometers. However, what really make these materials so special and attractive is not just their tiny dimensions but the appearance of new and unique physical and chemical properties and functionalities associated to such small scales. Plastic can become conductor and silver show antimicrobial properties. The study of size dependent properties, the sensibility to surface phenomena or the easiness to order in the space represent great challenges to understand these materials. The ability to control the structure and to manufacture nanomaterials is expected to allow the design of materials with the desired properties, in order to reach a large variety of applications where the size of particles results into highly beneficial properties [1]. Consequently, the interest in nanomaterials is also strongly promoted by technological and economical purposes. It has been estimated a high performance potential in many different fields. Distinct applications in optoelectronics, photovoltaics, photocatalitics, microelectronics, sensors, detectors, etc. are foreseen to generate a deep impact in our everyday lives, from the fabrics we wear till the capacity to heal illnesses like cancer, for example. Particularly, it is predicted a great success in the design of faster

computers, new modes of use and store energy, preservation of the environment or diagnosis and cure of diseases. It was already pointed out by R. Feynman, "there is plenty of room at the bottom" [2].

This race towards miniaturization is strongly linked to the development of the appropriate methodologies of synthesis, growth and characterization of nanostructures. In microelectronics, for example, structures with well-defined lateral dimensions lower than 100 nm are required in order to keep with the current rate of speed and storage density increase of our computers. The common techniques based on *top-down* approaches, such as conventional lithography, are reaching their limits. New and sophisticated upgrades, incorporating electron- and ion-beam writing, use of extreme violet radiation [3], etc. are showing their potential. They are "serial" nanofabrication techniques and, hence, slow and costly. Therefore, they will find extended practical use only if they are economically viable and scalable to industrial processes. Some other top-down methodologies such are microcontact printing or nanoimprint lithography are also being successful explored to overcome the "serial" characteristics of most techniques [4].

Alternatively and within this framework, *self-assembling* and *self-organizing* processes have attract the interest of scientists in the last years due to their ability to generate similar structures with narrow size distributions and high tendency to arrange into ordered matrices in a parallel fabrication mode, i.e. these nanostructures form spontaneously. It is a *bottom-up* approach, where the minimization of the energy of the system is the driving force for the spontaneous organization of the atoms, molecules, particles or other elements into these surprising structures. Nowadays, these processes have become an effective, promising and elegant route to sinterize a large variety of materials. Nonetheless, despite being a quite new strategy in the scientific community, spontaneous ordering is a common phenomenon in Nature [5, 6]. It ranges from atomic to cosmic scale, and applies to a large variety of systems, animate and inanimate. The dunes of the desert or the glaciers of the Antarctic are two examples from the macroscopic world; the organization in osseous tissue or the walls of some unicellular algae prove that these phenomena also takes place at nanometric scale [7, 8]. Technically, the definition of self-organization implies the existence of two basic properties, the system must be dissipative and no lineal [9]. This idea can be summarized through the differential equation

$$\frac{\partial \vec{u}}{\partial t} = \vec{k}\nabla^2\vec{u} + \vec{F}(\vec{u}) \qquad \textbf{Eq. 1-1}$$

where the vector **u** describes the behaviour space-time of a set of dependent variables, such as the concentration of chemical products or species, which can interact in accordance with no-lineal processes **F(u)** [10]. Therefore, from the point of view of theory of no-lineal dissipative

and dynamic systems, Eq. 1-1 is valid either to describe the skin spots of the leopard or the beating of a living heart. Both phenomena are also considered self-assemble.

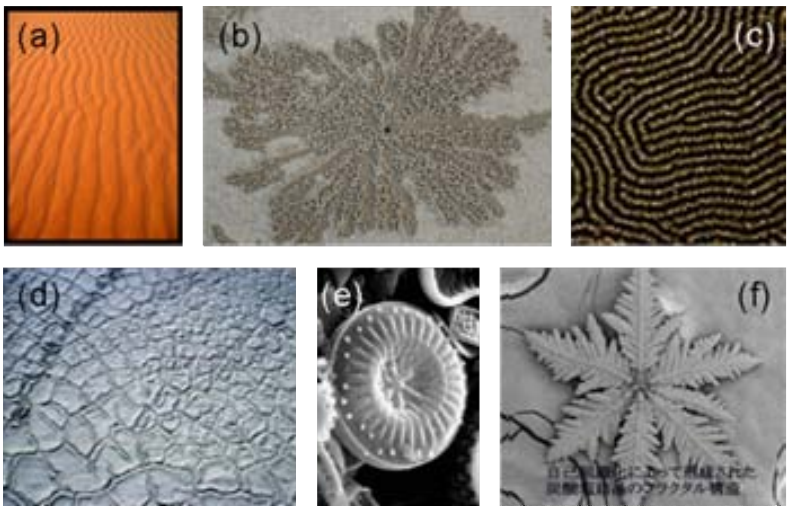

Fig. 1-1: Examples of self-organized patterns in nature: dunes in Sahara desert (a), sand balls made by a crab burrowing (b), silver nanowires (c), cracks in the clay (d), unicellular alga (d) and calcium carbonate crystal (f).

Self-organizing processes are technologically really simple, but as disadvantage in front of top-down approaches they present a lower control on the shape and size of the resulting structures. Even tough, in those technological applications where the uniformity between structures is more important than morphological and dimensional requirements, these phenomena arise as a very promising route for the low-cost nanostructuration of large areas. Moreover, they might enable to generate smaller nanostructures than those typically obtained with conventional top-down approaches.

It is especially remarkable the use of self-assembling processes in epitaxial growth, i.e. the ordered growth of a crystalline material A on top of a crystalline substrate B. When A and B are the same material, it is called *homoepitaxial growth*; when they are distinct specimens, it is named *heteroepitaxial growth* [11]. In the latter, the elastic strain induced because of the lattice mismatch between the deposited layer A and the substrate B plays a crucial role in the generation of nanostructures. Self-assembling processes in epitaxial growth have already been intensively investigated and applied in the semiconductor field [12-14]. Particularly, they have been proved to be very effective to generate quantum dots.

In the field of strain-induced nanostructures, it is common to refer as self-assembling processes to those which imply the formation of structures with narrow distribution of sizes. Just in the case where there exists an additional tendency towards order, one talks about self-organization.

1.2 Formation and evolution of 3D islands

In heteroepitaxial growth, the misfit between deposited material A and the substrate B leads to built up of elastic strain as film grows. At first stages, the formation of islands arises as the only coherent mechanism of elastic relaxation in heteroepitaxial growth on a substrate [15]. However, it must be taken into account that islands' formation implies an increase of the total surface of the system and, therefore, a change in its surface energy which in most of the cases results into an additional energetic cost for the system. Hence, the trade-off between surface energy and gain of elastic energy is the basic driving force for the transition from film to islands' growth.

The extensive and intensive investigation carried out in the heteroepitaxial growth in semiconductors can be used as model system to study self-assembling and self-organizing processes of nanostructures on solid surfaces and, particularly, the distinct energetic contributions present in island's formation.

The energy of an island in a dilute array of islands where interactions between them are negligible is generally considered as the sum of three contributions [15]

$$E_{island} = E_{surf} + E_{elast} + E_{edges} \qquad \textbf{Eq. 1-2}$$

where E_{surf} includes the surface and interface energy contribution, E_{elast} is the elastic relaxation energy and E_{edges} is the short-range contribution of edges. In subsequent sections, distinct energy contributions to E_{island} are explored in detail.

1.2.1 Surface and interface energy

Surface energy is a measure of the average behaviour of atoms on a surface, which provides useful information about growth processes. For example, the phenomenon of equilibrium facets plays a key role in determining the equilibrium shape of a crystal; therefore, structures which imply the formation of highly energetic surfaces will not be favoured or, simply, will not form.

Surface energy indicates the net change in the energy of a system because of the work that must be done to overcome the chemical bonds to create surfaces [11]. In general, there is an increase (reduction) of free energy associated in breaking (forming) bonds. Despite being the chemical bonding potential the basic contribution to the energy of a surface, there exist other features that contribute to it as well. Atoms in a surface might move with respect their bulk positions to restore the equilibrium present before the breakage of bonds, and they can even create new bonds with other atoms (surface reconstruction). Each reconstructed configuration represents a local minimum of surface energy. So, surface energy might be lower from the level predicted just considering bond contribution.

Moreover, atoms in a surface are in a distinct environment from those in the bulk. So, surface layer favours a lattice parameter distinct from that of the bulk in the directions parallel to the surface resulting in deformation [11, 15]. Since surface must adjust to bulk parameter, atoms in the surface are intrinsically stretched or compressed. Thus, surface energy also depends on the strain energy at each point. In contrast to liquids, solids are indeed not incompressible. Therefore, the energy required for the formation of a surface with a specific orientation is characterized by the surface energy scalar quantity γ, but also by the change in energy consequence of the deformation of the surface of the crystal, which is described by the stress tensor $\tau_{\alpha\beta}$. This dependence of surface energy on strain can be thought as a strain-induced renormalization of the surface energy.

Like free surfaces, the interfaces where two distinct materials join can also be characterized by an interface surface energy per unit of area, since nearly the same physical origin applies. In general, the interface energy density is lower than the sum of the free surface energy densities of the two materials in contact [11]. The importance of interfaces cannot be underestimated since they play a key role in many technological or biomedical applications as well as on islands' formation [16].

Values of intrinsic surface tensor are found either from first-principle calculations or from comparison with indirect data. Values of surface energy per unit area of a given crystallographic surface orientation are determined by the fine scale structure of the crystal, i.e. for example applying *ab initio* calculation [17, 18]. However, it is by far no trivial; even the surfaces of low-index are in general not reliably known. In the case where surface energies of the substrate and of the island are known and that of the interface, the surface energy contribution is easily calculated for a specific island shape. There exist methodologies to determine the equilibrium shape of free crystals on a substrate through geometric considerations of the classical Wulf analysis once corresponding surfaces energies γ_i are known [19-21]. Let's notice that the E_{surf} contribution in Eq. 1-2 considers the change in surface energy because of island's formation with respect to a 2D film.

In heteroepitaxial growth, a first common classification of growth modes in the thermodynamic regime is based on the surface and interface energies of the system. The growth of the material A on a material B is treated in analogous form to the consideration of surface tension of a liquid on a solid substrate [12, 13]. If the sum of the surface energy γ_A of the deposited layer and the interface energy γ_{AB} is lower than the surface energy γ_B of the substrate, $\gamma_A + \gamma_{AB} < \gamma_B$, the deposited material grows layer-by-layer (2D). In this mode, also named Frank-van der Merwe growth mode, the deposited layer completely wets the substrate [22].

Distinct configuration occurs when surface and interface energies satisfy $\gamma_A + \gamma_{AB} > \gamma_B$. In this case, it is energetically more favourable to grow just partially covering the substrate. As a result, three-dimensional (3D) islands form in the so called Volmer-Weber growth mode [23]. Nevertheless, in heteroepitaxial growth, the picture is not complete without considering strain energy, which plays a key role in islands' formation. For a strained layer, the growth might initially proceed layer-by-layer and then be followed by the growth of 3D islands, since the high strain energy of a thick layer can be lowered through islands' formation. That is referred as the Stranski-Krastanow growth mode [24]. Fig. 1-2 shows a schematic representation of these distinct growth modes in heteroepitaxial growth.

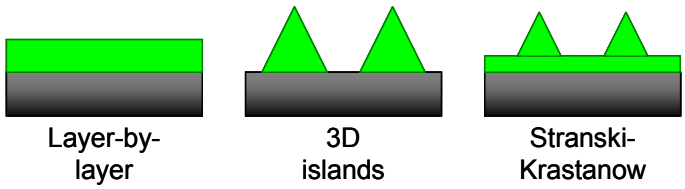

Fig. 1-2: Schematic representation of heteroepitaxial growth: 2D layer-by-layer or Frank-van der Merwe growth, 3D islands or Volmer-Weber growth and Stranski-Krastanow growth.

1.2.2 Elastic energy

In epitaxial growth, the atoms of the substrate provide a template for the positioning of the atoms of the deposited specimen. In heteroepitaxial growth, film has a stress-free lattice dimension a_F distinct from that of the substrate, a_S. Even though, the atoms of the deposited material position on top of the substrate trying to replay substrate's lattice parameter, resulting into an accumulation of strain energy. The mismatch strain can be expressed as

$$\varepsilon = \frac{a_S - a_F}{a_F} \qquad \textbf{Eq. 1-3}$$

and the total elastic strain energy due to lattice mismatch as [11]

$$E_{elast} = \frac{1}{2}\int_V \lambda_{ijkl}\,\varepsilon_{ij}\,\varepsilon_{ji}\,dV \qquad \textbf{Eq. 1-4}$$

where λ_{ijkl} is the array of the elastic constants and ε_{ij} is the non-uniform elastic strain field arising from the lattice mismatch. Thus, the elastic strain energy depends on lattice mismatch as $E^V_{elast} \sim \lambda\varepsilon^2 a_F^3$. The larger the misfit, the higher is the elastic energy of the system. Thus, a thin film deposited epitaxially on a substrate is usually unstable and the formation of interfacial nanoislands constitutes a mechanism to partially relax the system, since the upper lattice planes of the island can relax towards their intrinsic lattice parameter as it is illustrated in Fig. 1-3a [13]. The elastic relaxation strongly depends on island's shape and volume, $E^V_{elast} \sim V$.

Specifically, large elastic strain relaxation is in principally achieved as higher is the height-to-width ratio (Fig. 1-3b and c) [15].

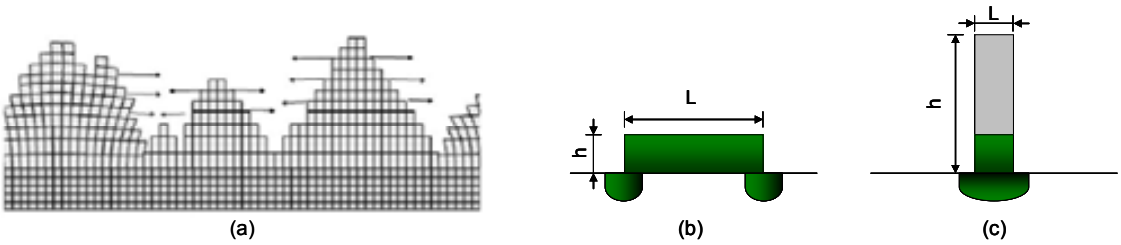

Fig. 1-3: Schematic representation of strain relief through the formation of coherently strained islands (a) [13]. Influence of island's shape on volume elastic relaxation (b,c), where the green area represents the region with high strain energy density. Weaker relaxation is achieved for islands with height-to-width h/L<<1 (b) as compared to those satisfying h/L>>1 (c) [15].

Till now, just elastic relaxation energy due to lattice mismatch has been considered. However, in an island with finite lateral edges, side facets allow further elastic relaxation of the system [15]. That is due to the discontinuity of the intrinsic surface stress tensor at island edges, which leads to the apparition of effective forces applied to island facets, $F_\alpha \sim \partial\tau_{\alpha\beta}/\partial r_\beta$. This constitutes another key point for the formation of interfacial nanoislands as a mechanism of elastic energy relaxation in contrast to strained films. These forces create an elastic strain field which elastically distorts the substrate lowering island's energy at the cost of some strain in the substrate. Formation of trenches around islands to relieve misfit strains has been observed [25, 26]. Further attention to substrate deformation is given in section 1.2.4. For the case of monolayer high islands or systems with planar islands with dimensions satisfying $a_F << h << L$, being a_F the lattice parameter and h and L the height and size of the island, respectively, the total force per unit length at the boundary of the island is

$$F_\alpha = \Delta\tau_{\alpha\beta}\, m_\beta = \sigma_{\alpha\beta}\, h\, m_\beta \qquad \textbf{Eq. 1-5}$$

where $\sigma_{\alpha\beta}$ is the elastic stress tensor of the film with in-plane components α,β, and m_β is a 2D unit vector normal to island's boundary. Fig. 1-4 shows a schematic representation of the heteroepitaxial growth of a rectangular strained-island; force monopoles are indicated.

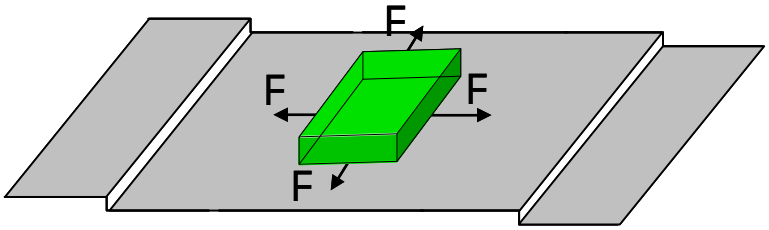

Fig. 1-4: Schematic view of the growth of an island in a heteroepitaxial system. Notice the surface force monopoles at island's edges.

Hence, for lattice mismatched systems with edges, the total strain field is the sum of two contributions, the lattice mismatch and the discontinuity of the intrinsic stress tensor $\tau_{\alpha\beta}$ at the edges [15]. Therefore, the elastic relaxation energy is the result of the combined performance of distinct sources of strain: elastic energy of the volume, energy of volume elastic relaxation due to tilted facets of island, interaction between strain due to lattice mismatch and discontinuity of intrinsic surface stress, etc.

There are distinct approaches to calculate the elastic relaxation energy of a strained 3D island; numerical finite calculations [27] or approximate analytic calculations are two methods. An example of the latter was proposed by Tersoff and Tromp [28], who derived an equation to describe the elastic strain energy of a 3D rectangular island with kinetically-limited height growth, where strain is assumed to not vary in z direction and its lateral sizes (*s*, *t*) are larger than its height *h*. Accordingly, the elastic relaxation energy of an island grown in an isotropic solid ($\sigma_{\alpha\beta}= \sigma_b$) can be written as

$$E_{elast} = -2\,c\,h^2\left\{a\ln\left(\frac{t}{\varphi\,h}\right)+b\ln\left(\frac{s}{\varphi\,h}\right)\right\} \qquad \textbf{Eq. 1-6}$$

where $c= \sigma_b^2(1-\nu)/2\pi\mu$, being ν the Poisson ratio and μ the shear modulus of the substrate; and $\varphi=e^{-3/2}\mathrm{cotg}\theta$, where θ is the angle between lateral island facets and the substrate. The substrate plus a reservoir of the deposited material strained to match the substrate in x and y direction, and free to relax in z was taken as energy reference.

1.2.3 Energy of a 3D interfacial island

Summarizing, the energy of a single island of volume V in a dilute array of islands can be more specifically written as [15]

$$E_{island}(V) = \left[(\Delta\Gamma)V^{2/3} - f_1\,\lambda\,\varepsilon_0^2\,V - \frac{f_2\tau^2}{\lambda}V^{1/3}\ln\left(\frac{V^{1/3}}{2\pi a}\right)+f_2\eta V^{1/3}\right] \qquad \textbf{Eq. 1-7}$$

The first term is the change in surface energy because of island's formation with respect to a film; it includes the renormalized surface energy due to strain energy, the formation of tilted facets, the disappearance of the planar surface area, etc. The second term is the energy of the volume elastic relaxation (E_{elast}^{V}) and the third term is the contribution of island's edges to elastic relaxation energy (E_{elast}^{edges}), being *a* the lattice parameter. The fourth summand is the always positive short-range contribution of edges, where η is a characteristic energy per unit length. Coefficients f_i are geometric factors. It must be noticed that the elastic relaxation energy (either volume or edges contribution) is always negative. However, the change in surface energy $\Delta\Gamma$ can indeed be positive or negative; $\Delta\Gamma>0$ implies a cost of energy for islands's formation to

happen, whereas $\Delta\Gamma<0$ results into additional gain of energy for the system through islands' formation.

In a dilute array of islands, where distances between islands are much larger than the island size itself, island's evolution to its equilibrium shape takes place faster than exchange of atoms between islands. Thus, there exists an equilibrium shape for each island's volume. The formation of one or another shape might depend on surface energies, strain and coverage among other parameters such as deposition or growth conditions. Since strain fields are concentrated around the base area of the island, upwards growth is a priori the most effective relaxation path [15, 17]. According to generalized Wulff-Kaishew theorem, relaxation of misfit strain enhances higher vertical aspects ratios as volume of strained-islands increases, together with sharpening of islands' crest [29]. However, lateral growth of islands has also been experimentally observed and theoretically predicted; anisotropic island's shape is treated in detail in section 1.2.6.2. Pyramids, huts or domes are some examples of morphologies typically observed in semiconductors [30-32]. It must be noticed that once the island is formed it can also experience shape transitions [31, 33, 34]. Transition from pyramid to dome-shaped islands is typically observed in Ge/Si(001) and InAs/GaAs(001) systems once islands grow beyond a critical volume [32, 35].

Nonetheless, it must be considered that volume elastic relaxation competes with introduction of misfit dislocations as a mechanism of strain relief of strained epitaxial layers [12, 36]. It has been showed that the barrier for the formation of 3D islands in Stranski-Krastanow configuration depends on misfit as ε^{-4}, whereas the barrier for nucleation of dislocations scales as ε^{-1} [12, 37]. Thus, island's formation is favoured in systems with high misfit strains. However, combined relaxation mechanisms can also occur. For example, $TiSi_2$ and $CoSi_2$ nanocrystals on Si(111) grow initially vertically with sharp apex, and above a critical height plastic strain relaxation occurs through the introduction of misfit dislocations at the interface, which leads to truncation of islands [38]. Strained islands are named *coherent*, whereas islands completely relaxed through dislocations are referred as *incoherent*; islands with intermediate degree of relaxation are called *semi-coherent*. Phase diagrams showing the preferred morphology in lattice-mismatched system Ge/Si as function of coverage and the ratio of surface energy and the energy of a dislocated interface have been build up [15, 39].

Like most of the approaches, all energetic description treated up to now refers to the T=0 K case. Despite high temperatures are essential for island's formation in most of the systems, just very few models consider temperature dependence. In a system where islands are allowed to equilibrate, they may show uniform sizes and shapes in the thermodynamic limit. Applying general concepts described above, the spontaneous formation of interfacial

nanoislands with uniform shape and size is a self-assembled process. For zero temperature, there is an infinitely sharp distribution of sizes with preferential island size N_0 determined through minimization of the total energy. However, as temperature rises the distribution broadens due to entropic contribution [40]. For a finite temperature, the optimum island size is given by

$$N_{opt} = N_0 - \frac{2\sqrt{N_0}}{c_2} k\,T \left(\frac{4\pi k\,T\,N_0^{7/2}}{c_2\,q^2} \right) \qquad \textbf{Eq. 1-8}$$

where q is the total coverage, and c_1 and c_2 are constants. Beyond optimum island's size, temperature influence can also be reflected on island's shape or through rounding of edges. For example, Ge pyramids and domes typically grow at temperatures above 550°C, whereas at lower temperatures huts easily form [33].

1.2.4 Interaction between interfacial islands

In many situations, islands are not in a dilute system but they elastically interact ones with the others. Therefore, Eq. 1-2 can be generalized to describe the energy of a single island in a dense array

$$E_{island} = E_{surf} + E_{elast} + E_{edges} + E_{int} \qquad \textbf{Eq. 1-9}$$

where E_{int} represents the interaction between islands. This last term is essential to explain self-organization processes, since a system of interacting islands is like a system of stress domains where the minimum of strain energy corresponds to a system of periodic domains [42-44]. Interaction between islands takes place due to long-range elastic interactions mediated via the substrate. The driving force for periodic order is the strain field generated by lattice mismatch and the discontinuity of the intrinsic surface stress $\tau_{\alpha\beta}$ at island edges [15]. Fig. 1-5b illustrates the finite element results of the deformation field of an arc-shaped island compressively-strained on a substrate [41]. The island must expand in the direction along the interface to fit the substrate lattice parameter. Because of the force that the island exerts on the substrate, substrate also expands in the same direction. To counteract this substrate extension, free substrate regions adjacent to island's edges compress. As a result, substrate regions around biaxial isotropic stressed islands are strained, which causes tendency of island to repel each other.

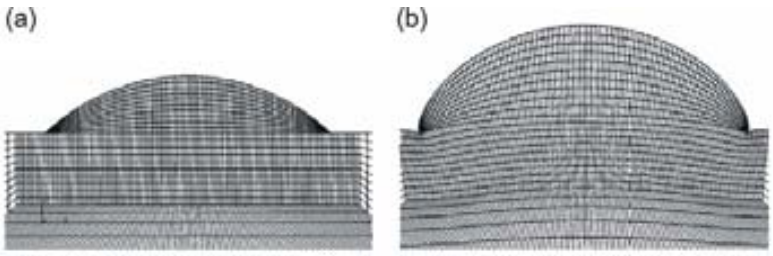

Fig. 1-5: Undeformed finite element mesh (a) and finite element results (b) of the deformation of an arc-shaped island on a substrate in compressive mismatch strain [41]. Notice substrate deformation at island's edges in (b).

When the separation between islands is larger than their own size, interaction between islands can be modelled by a dipole-dipole interaction [45]

$$E_{int}(R_i) = 2\pi\beta\sum_{i\neq j}\frac{R_i^2 R_j^2}{D_{ij}^3} \qquad \textbf{Eq. 1-10}$$

where R_j is the island's radius, D_{ij} the mean separation between island *i* and *j*, and $\beta=F^2(1+\nu)/2\mu$, being F the misfit strain-induced force monopole. Eq. 1-10 describes the repulsive interaction between islands in an elastic isotropic medium, which might result into self-organized arrays of islands [44, 45]. Nonetheless, in systems with strong elastic anisotropy, the direction of interaction between islands must be considered. More generally, dipole-dipole interaction between islands can be written then as [15]

$$E_{int} = \frac{C_o}{2\pi} V^2 \frac{B_1 + 15\, B_2\, (1 - 8 m_x^2 m_y^2)}{R^3} \qquad \textbf{Eq. 1-11}$$

where V is the island's volume, R is the distance between the two islands, $\mathbf{m}=(m_x, m_y)$ is the unit vector in the surface plane parallel to the direction between islands and B_1 and B_2 coefficients of the Green's tensor. For an elastic isotropic medium, $B_2=0$ and Eq. 1-11 reverts to Eq. 1-10. For an elastic anisotropic medium, Eq. 1-11 leads to attractive interaction between islands along elastic soft axis of the substrate, [100] and [010], which may imply the order of islands in chains parallel to these directions [15]. Resolve the exact interaction between 3D islands is in general complicated; despite that, there exist studies where forces responsible for maintaining self-organized vacancy lattices in Ag/Ru have been determined and quantified [46].

Besides inducing order, elastic interactions can also influence islands size distribution [45] or modify transition between islands' shape [31], for example.

1.2.5 Evolution of interfacial islands

Once the islands are formed, it is also generally expected that they will undergo Ostwald ripening [47]. It is a spontaneously thermodynamically-driven process which consists of the growth of some islands at expenses of others which shrink, i.e. small islands dilute and there is atomic diffusion towards large islands. Schematic picture of Ostwald ripening process is shown in Fig. 1-6. The energy of an atom placed at crystal surface is higher than when it is ordered and packed in its interior. Hence, large islands are generally energetically more favourable since they have lower surface area to volume ratio. This phenomenon is very beneficial to reduce the total area of the system in situations where the change in surface energy because of islands' formation is positive ($\Delta\Gamma>0$).

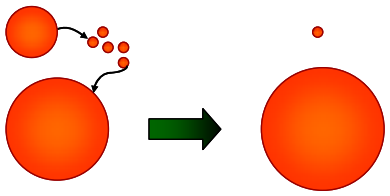

Fig. 1-6: Schematic representation of Ostwald ripening process.

Besides the incorporation of material through atomic diffusion (new deposited atoms, Ostwald ripening), island's volume can also increase through mechanisms of static [48] or dynamic [49] coalescence. The former mechanism considers the case where two islands grow independently (i.e. attachment of just deposited atoms, diffusion of atoms from other islands, etc.) and, as consequence of their expansion, they happen to touch and then they merge in a larger island. In the latter case, junction of islands occurs because of the diffusion of a whole island on substrate surface; once they meet, they also reconstruct into a larger island. Diffusion of clusters of atoms or vacancies on surfaces has been reported [50-52], the motion of 2D Ag islands on (100)Ag [49] or the lateral displacement of coherently strained 3D SiGe islands on (001)Si [53] are two examples.

In contrast to ripening or coalescence, it may instead form a uniform and stable array of interfacial nanoislands which do not undergo ripening. Details of this state are discussed in subsequent section.

1.2.6 Thermodynamic *versus* kinetic mechanisms

Till the moment, considerations of islands' formation have essentially based on thermodynamic arguments. Determination of the equilibrium shape of an island through minimization of the total energy of the system is an example of thermodynamic procedure [28, 54, 55]. However, kinetic mechanisms cannot be obviated. In fact, kinetics is also a basic approach to describe crystal growth, and it might be as well reflected on island's size and shape [56]. It must be distinguished between two kinds of situations [15]. On one hand, there is kinetics in an open system, where deposition of atoms and simultaneous evolution of interfacial structures proceed. In this case, if it exists a steady structure is consequence of particular growth kinetics but not of equilibrium. On the other hand, there is kinetics in closed systems, where the total amount of deposited material is kept constant because deposition has been interrupted; it is the typical situation that takes place during annealing. In this case, the kinetic evolution of nanostructures leads towards their thermodynamic equilibrium configuration. Thus, kinetic processes are essential to reach situations of thermodynamic equilibrium. Examples of kinetic parameters comprise anisotropies in atoms diffusion on a surface [57], different atom-to-facet

attachment barriers [56] or other barriers that atoms feel when moving on a surface or over steps and kinks [58].

After deposition, diffusion of material on the surface is required to form the nanostructures. The ratio between diffusion D and deposition rate R might determine whether the pattern growth is determined by kinetics (D<<R) or deposition occurs close to equilibrium conditions (D>>R) [59]. Metallic islands are an example of growth kinetics, while supramolecular self-assembly takes place close to equilibrium; the growth of semiconductor nanostructures normally takes place in intermediate D/R region. Distinct examples are shown in Fig. 1-7.

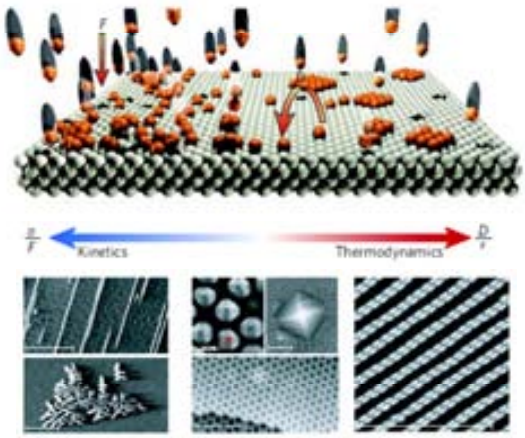

Fig. 1-7: Atomic scale view of growth processes on surfaces. Metallic islands are controlled by small diffusion to deposition D/R ratios (left-side); semiconductors nanostructures growth occurs at intermediate D/R values (centre) and supramolecular self-assembly takes place close to equilibrium condition at large D/R values (right-side) [59].

In strain-induced nanostructures' formation, growth and evolution, and even in crystalline and epitaxial growth in general, there exists a grand debate and certain controversy about which are the mechanisms determining thermodynamics and kinetics but, above all, about when dominate thermodynamic processes and when rule kinetic ones. Montecarlo simulations of the self-organized growth of quantum dots pointed out a crossover between kinetic and thermodynamic controlled regimes [40]. Initial stages of islands' growth seem to be controlled by kinetic mechanisms. Accordingly, many small islands form at low temperature, whereas at high temperature attachment to existing islands is more favourable and, thus, islands are large. Right after deposition, the system starts to equilibrate and it evolves to a thermodynamically controlled island size distribution. In this case, the average dots size decreases as higher is the temperature. Let's point out that in a thermodynamically-controlled size distribution the size of nanoislands decreases with increasing temperature. Conversely, island's size increases with temperature for the case of a size distribution dominated by kinetics.

Other controversial thermodynamic *vs.* kinetics examples include bimodal distributions of islands under determined growth conditions [25, 32, 60, 61], the formation of stable 3D

islands or the formation of in-plane elongated structures. These two latter cases are analyzed in detail next.

1.2.6.1 Stable 3D interfacial nanoislands

Formation of stable 3D islands with narrow size distribution and absence of Ostwald ripening are a typical illustration of thermodynamic-kinetics debate. Experimental control over the conditions where this behaviour takes place has resulted to be very fruitful to generate quantum dots for example for laser applications [62]. Therefore, knowledge and comprehension of mechanisms leading to the spontaneous generation of arrays of uniform nanoislands might provide an appealing tool to design nanostructured templates. Thermodynamic theories have proved the existence of a parameter region where the equilibrium of a system with 3D strained islands corresponds to a periodic array of identical islands. In contrast, kinetic theories attribute the existence of a stable narrow size distribution of islands' to self-limiting growth processes which drive large islands to grow more slowly than smaller ones.

From a thermodynamic point of view, if the change in surface energy due to islands' formation is lower than the contribution of edges to elastic relaxation energy, equilibrium condition (i.e. minimum of total energy) is satisfied if all islands adopt an optimum island size D_{opt} [44]. So, under these conditions, an array of identical islands of size D_{opt} is stable and ripening does not occur. If this condition is not fulfilled ($\Delta\Gamma > E_{elast}^{edges}$), there will exist tendency towards continuous ripening. From kinetic perspective, two mechanisms were proposed by Barabasi *et al.* [63] to explain this behaviour. First, detachment of atoms from islands is enhanced in large islands since strain fields are larger. Second, these strain fields generate net currents of atoms away from the island. As a result, growth rate of large islands is slowed down and nucleation of new islands is promoted leading to the formation of self-assembled islands with stress-induced narrow size distribution.

Let's point out that these models refers to the case of T=0 K, and the landscape might be drastically modified at typical experimental temperatures of growth and anneal. Statistical models introducing the influence of temperature and coverage have pointed out the existence of a critical temperature above which unstable ripening would occur, and pyramids or domes are anymore equilibrium nanostructures in this parameter region [60].

1.2.6.2 Anisotropic-shaped interfacial nanostructures

Rectangular hut clusters has been often observed after firstly reported by Mo *et al.* during first stages of growth of Ge on silicon [30]. Some examples of formation of elongated nanostructures include the systems GaAs/Si(100) [64], Ge on Au-patterned Si [65], Ag/Si(001) [28], $CoSi_2$/Si(100) [38, 66], Au/Ag(110) [67], Pd/$SrTiO_3$(100) [21], etc. Some cases are

illustrated in Fig. 1-8. Both energetic and kinetic arguments have been proposed to explain the origin of anisotropic island's formation. In this section, we outline some of these points of view.

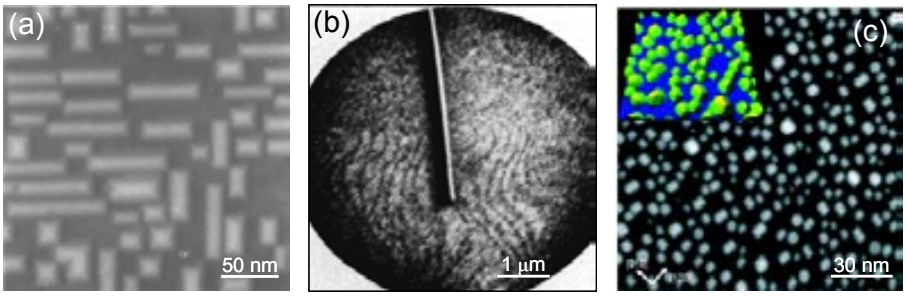

Fig. 1-8: Examples of interfacial nanoislands with high lateral aspect ratios in heteroepitaxial systems Ge/Si(001) [30] (a), Ag/Si(001) [28] (b) and Pd/STO(001) [21] (c).

Tersoff and Tromp [28] analyzed the equilibrium shape of strained-islands of fixed height. Minimization of the island's energy density (E/V) with respect to their lateral sizes *s* and *t* yielded to an optimal isomorphic square island's shape of size α_o, dimension which depends on strain and surface energies. For sizes beyond α_o, island might elongate in one direction and shrink to α_o in the orthogonal direction. Adopting a rectangular shape with width α_o, the island gains at least half of its optimal elastic relaxation energy. The corresponding dependence of E/V and lateral sizes *s* and *t* as function of island's base area A are depicted in Fig. 1-9a and b, respectively. Whereas these predictions seem to fit with some experimental results [66], they do not exactly agree with the anisotropic shape of other islands [38]. The equilibrium shape anisotropy of strained-nanoislands has been more recently studied by Li *et al.* [68], who found that strain leads islands to a great anisotropy as their size increases. Strictly speaking, Li *et al.* considered the energy of a 2D rectangular island; but their analyses are as well applicable to 3D islands with limited height growth, replacing edges by facets, etc. In this case, island's anisotropic shape is also explained through a competition between surface and elastic relaxation energies. A spontaneous shape instability will occur in strained-islands with isotropic surface energies: for smaller sizes, islands are isomorphic and, above a critical size D_c, they adopt a rectangular shape by elongating in either one of the two orthogonal directions with two degenerate minima (Fig. 1-9c). In the case of anisotropic surface energies, the symmetry in elongation along one of two directions is broken and elongation would solely occur in the direction of lower E_{surf} to minimize both surface and strain energies. In this case, island will adopt an anisotropic shape since nucleation (Fig. 1-9d). Nucleation of an island in a pit can be a mechanism of breaking the surface energy isotropy of facets and enhance island's elongation [33]. Experimental evidence of the model proposed by Li *et al.* [68] has been used in vacancy islands on the Ge(001) surfaces to extract the surface stress anisotropy of the system [69]. In Fig. 1-9, it is observed that the lateral aspect ratio of islands increases with size. Shchukin *et al.*

[70] claimed that an array of strained elongated nanostrauctures with positive surface energy contribution and elastically interacting between them might be unstable to Ostwald ripening.

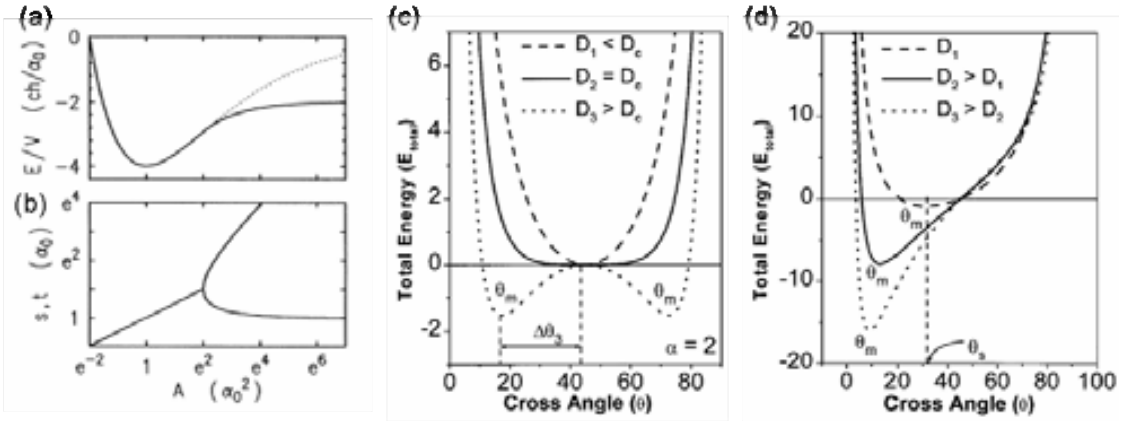

Fig. 1-9: Energy per unit volume E/V (a) and width *s* and length *t* (b) *vs.* island's area *A* for a strained 3D island with limited height growth [28], dotted-line shows the energy if island remained isomorphic. Total energy of strained 2D islands *vs.* θ≡arctan(s/t) showing the strain-induced shape instability for islands with isotropic (c) and anisotropic (d) step free energies [68].

On the other hand, elongation of islands can also be explained by different adatom-to-facet attachment barriers which are promoted by kinetic instabilities. Voigtländer gave direct experimental evidence of self-limiting growth of Ge huts on (001)Si and reported corresponding kinetic model [12]. Jesson *et al.* [56] pointed out the existence of an energy barrier to complete a facet related to the strain energy distribution in the island. The energy barrier of a facet of size *s* increases as increasing *s* and misfit strain; resulting in a self-limiting growth effect. Accordingly, elastic interaction or other sources of strain modulation in the neighbourhood of the island results into differences in the energy barriers of distinct facets, leading the island to an anisotropic shape. Once the island is anisotropic, the basal stress concentration facilitates the attachment of atoms on short facets yielding to continuous elongation of the island. Similar kinetically-limited mechanism has been observed in the formation of surface grooves from pit instabilities in annealed SiGe/Si(100) [71].

1.3 Application of self-assembling processes in different materials: oxides

For decades, self-assembling and self-organizing processes have attracted grand scientific and technological interest to grow semiconducting interfacial nanostructures [12, 13]. The growth of Si_xGe_{1-x} on Si(001) is a typical example of a well-studied system [31-33, 54, 60]. The extensive investigation carried out in semiconductors has lead to the development of innovative devices based on quantic phenomena of new structures such as nanodots or nanowires. As a result, there exist nowadays an extensive knowledge about growth of a large variety of semiconductor nanostructures with high control over size, morphology, density and

order [12, 13]. So far, self-assembling and self-organizing based methodologies have started to spread to other emerging fields such as metals [21, 72, 73] or molecules [59, 74], and recently to epitaxial oxides.

Despite research on self-assembled oxide nanostructures has been limited till the moment, there is an increasing interest focused on these materials due to the tendency observed in some oxides to grow forming arrays of uniform 3D nanostructures which foresees an important potential for the implementation of new devices in fields such as magnetism, ferroelectricity, ferromagnetism, colossal magnetoresistors or superconductivity [75-79]. Therefore, study of self-assembling and self-organizing processes on oxide materials constitutes both a scientific and technological challenge. Capabilities to grow oxide nanostructures have already been proved either using physical or chemical deposition routes [79-82]. Most investigated approaches are based on morphological instabilities induced in strained thin films, either after high temperature annealings or as a result of the deposition of ultrathin films [76, 81, 83]. Other routes to nanostructure oxide surfaces deal with segregation of materials in excess in the thin films [84] or microemulsion aided methods [85].

Examples of investigated self-assembled oxide nanostructured systems are varied and include, for example, morphological instabilities occurring during post-deposition thermal annealing in yttria-stabilized zirconia (YSZ) [83] or CeO_2 thin films grown on sapphire [76], spontaneously ordered Ce-doped Gd_2O_3 (GDC) nanoislands formed after the spallation of GDC films grown on YSZ single-crystals [86], islands' growth in highly mismatched systems such as CaO/MgO (ε=14.2%) and SrO/MgO (ε=22.5%) [87], evolution of $SrRuO_3$ nanostructures from ripples to nanowires as function of coverage [80], formation of semi-coherent $SrZrO_3$ pyramids on $SrTiO_3$ (STO) [88], nucleation of $SmY_2Ba_3O_7$ along STO vicinal substrate steps [89], self-ordered formation of $CoCr_2O_4$ pyramids and huts on $MgAl_2O_4$ with well-defined {111} facets [79], Stranski-Krastanov-like growth mode of (111)Fe_3O_4 islands on a (111)FeO wetting layer grown after iron evaporation on Ru and Pt substrates [90], etc. Some of these examples are illustrated in Fig. 1-10.

Till the moment, research carried out in oxides above all focuses on the generation of ferroelectric nanostructures, specially of $PbTiO_3$ [81, 82, 91] and $Pb(Zr_xTi_{1-x})O_3$ (PZT) [77, 92]. Interest in these materials lies on the impact that may have on future development of non-volatile ferroelectric random access memory (FeRAM) [93-95] and mass-storage media [96]. Common top-down approaches are already facing difficulties to generate ferroelectric nanostructures with lateral sizes below ~50 nm and, additionally, advanced techniques based on electron beam or focused ion beam might damage sidewalls of fabricated ferroelectric

nanodevices. So, bottom-up approaches based on self-assembling processes represent an important alternative route. Distinct studies of the influence of coverage and growth temperature have been carried out [77, 81, 92], showing the capabilities of self-assembling methodologies to grow well-defined oxide nanostructures with good ferroelectric properties [77, 91].

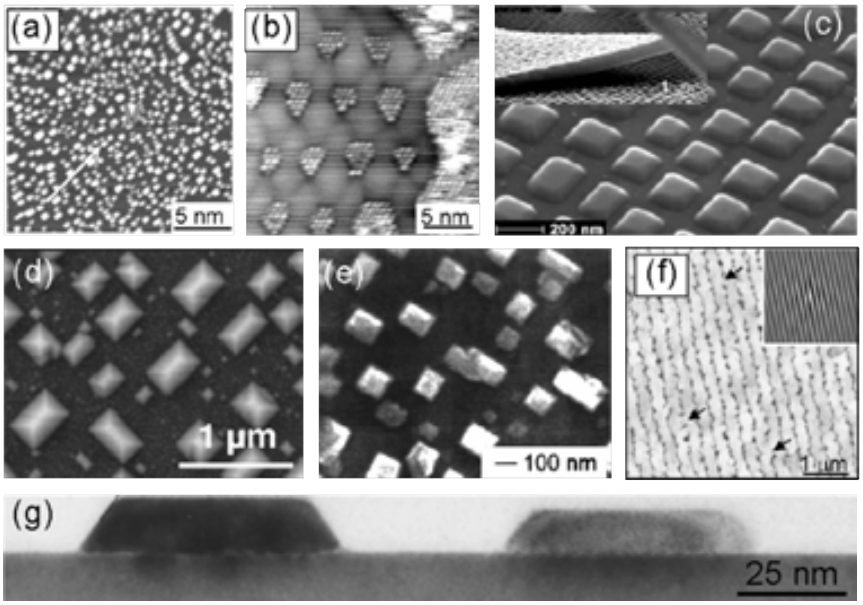

Fig. 1-10: Examples of systems with interfacial oxide nanostructures grown following a bottom-up approach: nanoislands on CeO_2 film grown on sapphire by PLD after high-temperature O_2 annealing [76] (a); (111)Fe_3O_4 domains embedded in a (111)FeO film [90] (b); self-ordered GDC nanostructures on (001)YSZ formed after the spallation of a GDC film (the inset shows the spalled film) [86] (c); self-organized nanopyramids and nanohuts of $CoCr_2O_4$ on $MgAl_2O_4$ deposited by sputtering [79] (d); self-organized Bi-containing nano-electrodes formed by segregation during the epitaxial deposition of a Bi-rich $Bi_4Ti_3O_{12}$ layer by PLD [84] (e); coalescence of $SrRuO_3$ islands into wires on $LaAlO_3$ substrates [80] (f); cross-sectional TEM images of 3D CeO_2 nanoislands on sapphire grown by PLD [76] (g).

Point-ended and truncated pyramids [81, 86], domes and superdomes [83, 92] and even shape instabilities leading to highly in-plane elongated nanostructures [82] are examples of typical semiconductor shapes that have found an analogous to oxide nanoislands. Moreover, some theoretical models developed to explain semiconductor nanostructures formation and characteristics have also been proved to apply to oxide materials [76, 81, 92]. Nonetheless, there is not always a direct correlation between semiconductor and oxide nanostructures [79]. Hence, growth of complex oxides might lead to new self-assembled and self-organized nanostructures showing innovative and interesting properties and functionalities not necessary predictable from the intensively investigated growth of semiconductors.

1.4 Chemical solution deposition (CSD), a new path towards the growth of interfacial nanostructures

1.4.1 CSD: preparation route

The use of chemical solution deposition (CSD) arises as an alternative low-cost methodology to vacuum related techniques for the growth of thin films in general and to nanostructure surfaces in particular. CSD has already been proved to succeed in the epitaxial growth of complex oxide films ($Pb(Zr,Ti)O_3$, $(Ba,Sr)TiO_3$, $BaZr_xY_{1-x}O_3$, $(La,Sr)MnO_3$, $YBa_2Cu_3O_7$, etc.) with many distinct functionalities (ferroelectrics, dielectrics, protonic and electronic conductors, high temperature superconductors, etc.) [97-99]. Interest in CSD is mainly based on the capabilities to obtain highly homogeneous solutions at molecular level, good control over the final stoichiometry of the product, low-cost and potential scalability to industry.

A typical CSD process is based on the preparation of a homogeneous solution with the desired concentration of cations, which is next spread over a substrate. Distinct coating techniques include spin-coating, dip-coating or spray-coating. Then, the sample is heat treated. At low temperatures (300-400^{o}C), it takes place the removal of the organic material (pyrolysis) resulting into the formation of an amorphous layer. At much higher temperatures, heat treatment leads to the densification and crystallization of the amorphous film into the desired oxide phase [100, 101].

The choice of precursor chemical must consider adequate solubility in the solvent to obtain a stable coating solution, acceptable wetting of the substrate, do not leave undesired residues after pyrolysis and do not form cracks or other non-uniformities during thermal processing, among other factors. Consequently, metal-organic compounds are very appropriate since their solubility in either polar and non-polar solvents can be regulated through modification of the organic part of the molecule, and because the pyrolysis of the organic fraction in oxidizing ambient atmosphere does not leave residue [102, 103]. Particularly, carboxilates precursors are usually selected in the so called metal-organic decomposition (MOD) route. Other chemical paths include sol-gel processes [104] or hybrid routes [105], for example.

A common coating technique, and the one used throughout the present work, is based on spin-coating. It involves the deposition of the solution on the substrate, which is then rapidly accelerated to a determined angular velocity at which it remains a certain time. During acceleration and rotation, the solution is homogeneously spread over the substrate's surface, and the excess of solution is expelled. These processes are the result of the presence of centrifugal and viscous forces; the rheological parameters of the solution are as well critical. Hence, the final thickness of the precursor solution can be mainly controlled through angular speed,

spinning time, viscosity and wetting angle of the solution and concentration of the solution. As disadvantage, spin coating exhibits a notable sensitivity to environmental conditions, i.e. humidity might influence the chemistry of the solution and evaporation rate, and modify the quality of the resulting film. Hence, control of environmental conditions during deposition is very important.

Transition from amorphous layer to crystallization occurs through nucleation and growth processes. In solution-derived processes, nucleation and growth can be treated as crystallization in traditional glasses [103]. From a thermodynamic perspective, the driving forces governing this transformation are the energy differences (ΔG_V) between these two states, i.e. amorphous and crystalline [100]. Therefore, ΔG_V is critical to determine the energy barriers and rate of nucleation of distinct crystalline phases. Fig. 1-11 displays a schematic diagram of the free energies of a CSD derived amorphous film and a crystalline perovskite phase, where the difference between both curves is indicative of the ΔG_V barrier.

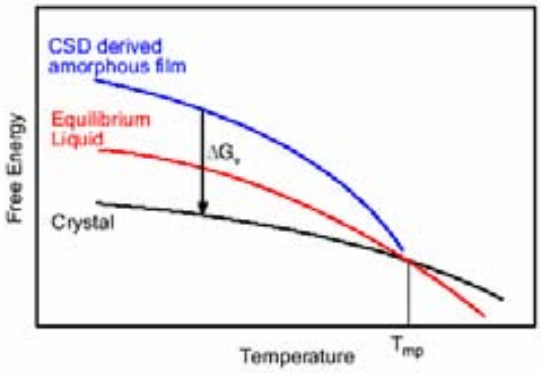

Fig. 1-11: Schematic diagram of the thermodynamic driving force ΔG_V for crystallization as function of temperature. The free energies of a CSD-derived amorphous film, the ideal supercooled liquid and a crystalline perovskite phase are plotted [99, 100, 106].

The energy barrier for homogeneous nucleation (crystals nucleate in all points of the amorphous film because there exist no preferential sites) and its dependence on driving force is given by [100]

$$\Delta G^*_{homo} = \frac{16\pi\gamma^3}{3(\Delta G_V)^2} \qquad \textbf{Eq. 1-12}$$

and for the case of heterogeneous nucleation (crystals nucleate at film/substrate interface)

$$\Delta G^*_{hetero} = \frac{16\pi\gamma^3}{3(\Delta G_V)^2} f(\theta) \qquad \textbf{Eq. 1-13}$$

where γ is the interface energy and $f(\theta)$ a function related to the contact angle θ, which for the case of an hemispherical nucleus takes the form $f(\theta)=(2-3\cos\theta+\cos^3\theta)/4$. Enhancing heterogeneous nucleation in front of homogeneous nucleation is crucial in those systems where

a particular orientation of the crystal is required, as it is for example the case of epitaxial growth of thin films or interfacial nanostructures.

Crystallization driving force ΔG_V depends on temperature (Fig. 1-11). Since the thermal energy available to the system is modified via heat treatment, driving forces determining nucleation events may also change with heat treatment temperature and, consequently, also does the resulting microstructure. As temperature rises, more thermal energy becomes available to surmount nucleation barriers of different kind of events and, thus, distinct populations arise. Particularly, at high temperatures, heterogeneous nucleation events become more important. Dependence of nucleation with temperature implies that crystallisation usually already begins during the heating to growth temperature.

1.4.2 Use of CSD for the generation of interfacial nanostructures

All examples shown in previous sections have in common the use of the path towards energy minimization as the driving force for the generation of self-patterned arrays of nanostructures with similar shapes and sizes. Nevertheless, deposition techniques used to generate these interfacial nanostructures are varied. Both physical and chemical deposition routes have been proved to be highly efficient. Particularly, the deposition techniques more frequently used for the growth of semiconductor nanostructures are molecular beam epitaxy (MBE) [25, 31, 36, 107] and chemical vapour deposition (CVD) [108]; despite other techniques such as liquid phase epitaxy (LPE) are as well used [109]. In oxide materials, pulsed laser deposition (PLD) [76, 80, 84] and radiofrequency magnetron sputtering [79, 86] are among most used techniques for the generation of oxide nanostructures; although some examples using MBE [89] or metal-organic chemical vapour deposition (MOCVD) [82] have also been reported.

CSD has already demonstrated its capabilities to successfully grow epitaxial thin films of complex oxides. However, its application on the generation of interfacial self-assembled oxide nanostructures has been scarcely investigated. One of the most common approaches consists of taking advantage of morphological instabilities experienced by strained thin films as a source of nanostructure generation. Below a critical thickness, continuous films might not be thermodynamically stable and they might break during high temperature heat treatments yielding to uncover of the substrate [81]. Till recently, these features were considered undesired side effects which occurred during the growth of heteroepitaxial thin films. Nowadays, they are being intensively explored for the generation of interfacial nanoislands. It is a thickness dependent phenomenon driven by the excess of free energy of a complete thin film with respect

to a layer just partially covering the substrate. The free energy is minimized through the development of holes that expose the substrate and lead to the apparition of free surfaces with lower free energy [87, 110]. At the same time, interfacial area is reduced and, thus, it is interface energy. In $PbTiO_3$ thin films elaborated by CSD spin-coating on STO single-crystals, this behaviour has been observed below a nominal thickness of ~80-100 nm [81, 111]. Formation of outgrowths emerging from the CSD-films after high temperature annealings has been recently observed in our group as another source of surface nanostructuration [112].

Since in CSD the amount of deposited material is a function of precursor solution, the formation of oxide nanoislands can also be achieved using ultradilute solutions [77]; that is, through the deposition of ultrathin films. In this case, the very first stages of islands' nucleation are studied. The former two strategies (morphological instabilities, outgrowths) normally results into larger islands (~100 nm) and, consequently, the use of highly dilute solutions arises as a more promising approach for the generation of templates with high density of interfacial nanodots and, thus, this has been the route used in the present work. .

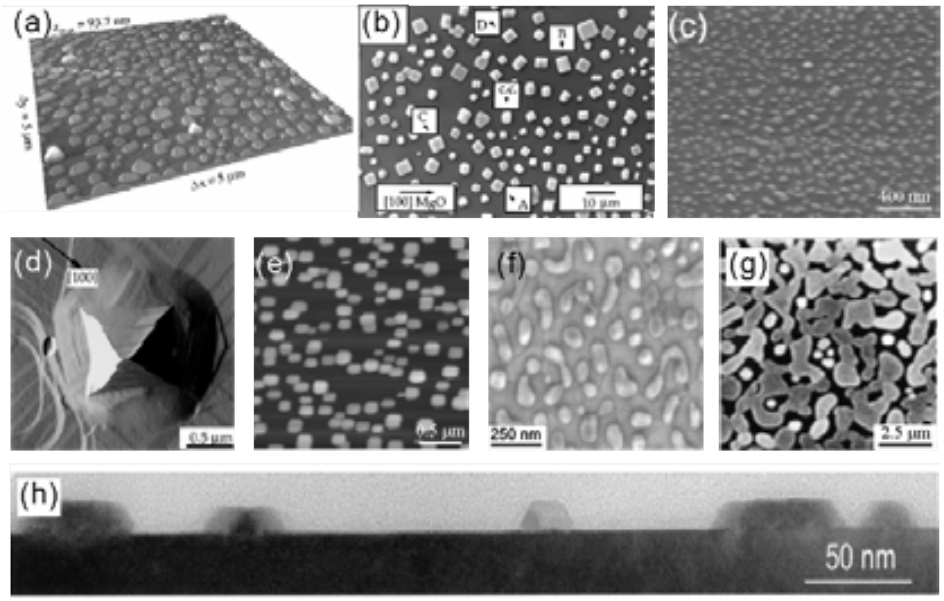

Fig. 1-12: Examples of interfacial oxide nanostructures grown by CSD: YSZ nanoislands on sapphire [83] (a); SrO film broken into cubic islands on MgO [87] (b); PZT islands grown from ultradiluted precursor solution concentration [77] (c); faceted $PbTiO_3$ island [81] (d); PZT superdomes on STO [92] (e); $PbTiO_3$ grains grown on $Si/SiO_2/TiO_2/Pt$ substrate [91] (f); interconnected (001)-oriented zirconia islands and small isolated grains on sapphire [113] (g); interfacial PZT islands on STO [77] (h).

Examples of shape instabilities induced in CSD-prepared thin films include the growth of 40 nm thick continuous epitaxial $SrZrO_3$ films on STO substrates which results in the formation of pyramid-shaped isolated nanoislands after posterior heat treatments at high temperature [88]. Polycrystalline YSZ films deposited by sol-gel dip-coating on sapphire substrates also split into islands; in this case, flat-top, dome-shaped or tilted flat-top islands' morphologies are observed to be correlated with step morphology of the substrate [83]. In

ferroelectrics, use of ultradiluted precursor solutions leads to the formation of PZT islands on STO showing a relative narrow size distribution with height ~9 nm and lateral sizes ~50 nm when annealed at 800^{o}C; however, better defined and larger pyramids are obtained after annealing at 1100^{o}C as consequence of the enhanced atomic mobility achieved at higher temperatures [77]. Few other examples of CSD-prepared ferroelectric nanostructures have also been reported, indicating the viability of this bottom-up approach based on CSD for the generation of ferroelectric devices [91, 92, 114]. Fig. 1-12 shows several examples of interfacial oxide nanostructures prepared by CSD.

1.5 Superconductivity and templates with interfacial self-assembled oxide nanoislands

The recent and increasing interest in the generation of templates with self-assembled interfacial oxide nanoislands basically bases on the potential capabilities to develop new applications derived from the emerging and attractive properties and functionalities related directly or indirectly to these oxide nanostructures. For example, in ferroelectrics materials, interfacial $PbTiO_3$ nanostructures with sizes below 15 nm have been fabricated through CSD bottom-up approach, sizes much smaller than those typically obtained following top-down methodologies. The ferroelectric behaviour shown by grains larger than 20 nm evidences the possibility to prepare, for example, ferroelectric memories of high densities [91]. The lack of long-range order presented by these nanostructures is being overcome with the use of a pre-patterned templates which directs the nucleation of $PbTiO_3$ islands [114].

In the superconductor field, it has been shown that vacuum deposited metal or oxide nanoparticles on a substrate might modify positively the dependence of critical current densities with magnetic field of superconductor $YBa_2Cu_3O_7$ (YBCO) thin films grown on top [115-117]. It is another example of a promising performance of interfacial oxide-derived nanostructures.

In the framework of this thesis, besides the basic scientific interest in the study of the generation of strain-induced oxide nanostructures by CSD, from a more technological point of view we investigated the potential application of these nanostructured templates on the improvement of superconducting properties of YBCO thin films also prepared by means of chemical solutions.

1.5.1 The phenomenon of superconductivity

Superconductivity is a phenomenon displayed by certain materials when they are cooled below a critical temperature T_c, which is characteristic of each material. One of the most outstanding properties of these materials is their capacity to transport current without dissipation

below T_c; i.e., they have no electrical resistance at $T<T_c$. In the framework of microscopic BCS theory (Bardeen-Cooper-Schrieffer, 1957) [118], this property is explained by the coupling of electrons into pairs (known as Cooper pairs) through interactions with the crystal lattice (phonons). Paired electrons do not behave as single electron fermions, but they act like bosons which can condensate in the same energy level. Consequently, Cooper pairs can move coherently in the crystal without dissipation. The wave function that describes all Cooper pairs, $\psi(r)$, varies within a distance determined by the coherence length $\xi(T)$ [119], being then ξ one of the most relevant parameters in superconductivity.

Another of the characteristic properties of superconductors is the expulsion of the interior magnetic field when they are cooled below T_c. Expulsion of the magnetic field is achieved though the induction of screening supercurrents and the phenomenon is known as Meissner effect [119]. These currents penetrate in the superconductor a distance characterized by the penetration depth $\lambda(T)$, leading to the exponential decay of the magnetic field from the outside down to the zero value inside.

Hence, there exists two characteristic lengths in superconductor materials, $\xi(T)$ and $\lambda(T)$. The ratio between them, $\kappa=\lambda/\xi$, classifies superconductors in two families: type I ($\kappa\leq\sqrt{2}$) and type II ($\kappa\geq\sqrt{2}$). For the former, the interface energy between a normal region and a superconducting region is positive. For the latter, it is negative and, consequently, type II superconductors favour the formation of this kind of interfaces. Most of superconducting elements are type I except niobium and vanadium, whereas the great majority of superconducting compounds like NiTi, Nb_3Sn, $Mo_{82}Si_{18}$ or cuprates are type II superconductors.

Type I superconductors are characterized by the thermodynamic magnetic field H_c. Above H_c the material is found in the normal state, and crossing $H_c(T)$ it undertakes a first order transition to the superconducting state. So, below H_c they expulse the interior magnetic field and, in this Meissner state, the superconductor behave as a perfect diamagnet. Fig. 1-13a shows an schema of the phase diagram of a type I superconductor.

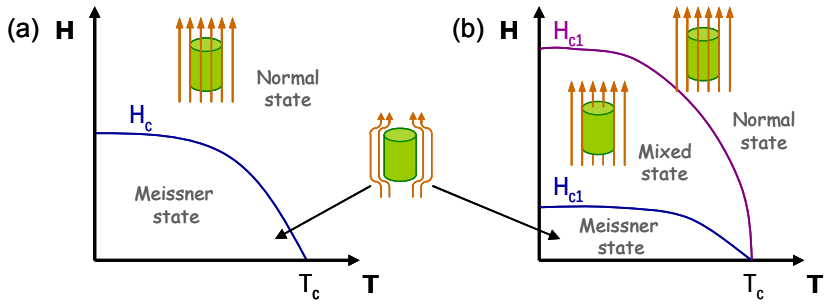

Fig. 1-13: Schematic representation of the magnetic phase diagram of type I (a) and type II (b) superconductors.

Type II superconductors are just found in Meissner state for magnetic fields below the critical field H_{c1}. For $H>H_{c1}$, the magnetic flux is not longer expelled; instead, it penetrates from superconductor surface to its interior as tubes of quantized magnetic flux called vortices. This region is known as mixed state and it holds till the magnetic field H_{c2}. Fig. 1-13b shows the corresponding schema of the magnetic phase diagram. Vortices consist of a core in the normal state of radius ξ, where the density of Cooper pairs is null (superconducting order parameter $|\psi(r)|$ is zero), and circulating superconducting currents which penetrate a distance λ from the centre of the vortex into the superconductor. These currents generate a flux quantum in each vortex, $\Phi_o = 2.07 \cdot 10^{-15}$ T·m^2, so that the magnetic field is maximum at the centre of the vortex. Since each vortex supports one quantum flux, the magnetic flux inside the superconductor in the mixed state is quantized, i.e. $B=n\Phi_o$. Fig. 1-14 schematizes the transversal section of a vortex. The presence of vortices ensures an elevate number of normal-superconductor interfaces in type II superconductors.

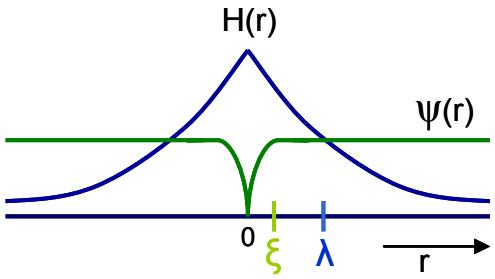

Fig. 1-14: Schematic representation of an Abrikosov vortex; characteristic penetration depth λ and coherence length ξ are indicated.

Vortices interact repulsively between each other. Consequently, they order in an hexagonal lattice (of lattice parameter a_o) to minimize the energy of the system. This vortex lattice is called Abrikosov lattice [121]. Fig. 1-15 displays a visualization of it obtained by magnetic Bitter decoration [120]. As the applied magnetic field increases, the density of vortices n inside the superconductor also increases according to $B= n\Phi_o$. The distance between vortices scales as $a_o \sim B^{-1/2}$. When the magnetic field H_{c2} is reached, the cores of neighbouring vortex overlap and the material transits to normal state.

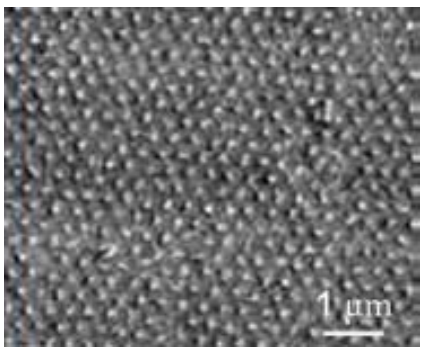

Fig. 1-15: Abrikosov lattice of vortex visualized by Bitter decoration [120].

When a current **J** circulates in a superconductor material in the mixed state, it arises a Lorentz-like force acting on the vortices [119], $\mathbf{F}_L=\mathbf{J}$ x **B**. As a result, the flux lines move within the superconductor and it appears an electric field $\mathbf{E}=\mathbf{v}_l$ x **B**, where $\mathbf{v}_l$ is the local velocity of flux lines. As soon as vortices start to move across the superconductor, there is dissipation of energy and the material is no longer able to transport current at zero electrical resistance. To avoid dissipation, vortices must keep pinned (i.e., $\mathbf{v}_l=0$). Vortices can be fixed in inhomogeneities (defects) of the material. Crystalline defects such as oxygen vacancies, precipitates of non-superconducting phases, dislocations, twin boundaries, etc. may act as pinning centres. A vortex placed in a lattice defect can reduce its free energy, since these sites are non-superconducting like vortices' core. For core pinning, the most effective pinning sites are those of similar dimension to vortex core, i.e. ξ.

The maximum current density that can flow in these materials without dissipation is the critical current density $\mathbf{J}_c$. It is defined as the current that produces a Lorentz-like force $\mathbf{F}_L$ equal to the mean pinning force per unit volume $\mathbf{F}_p$ exerted by defects on the flux lines, i.e. $\mathbf{F}_p=\mathbf{J}_c \wedge \mathbf{B}$. So, when J exceeds J_c, the superconductor switches into a dissipative state still within the superconducting state. It is the case of flux creep or flux flow phenomena, which will be revised in chapter 7.

1.5.2 High temperature superconductors, $YBa_2Cu_3O_{7-x}$

Superconducting materials can be classified as low temperature superconductors (LTS) and high temperature superconductors (HTS). For the former, the formation of Cooper pairs can be satisfactory explained by the microscopic BCS theory [118]. Nb-Ti alloy (T_c=9 K) and Nb_3Sn (T_c=18 K) are examples of LTS. For the latter, the coupling of electrons into Cooper pairs cannot be explained just considering electron-phonon interaction because of high T_c values. Distinct theories have been proposed to explain the origin of charge attraction in HTS, but it still remains an open issue.

Among HTS, cuprates is the most relevant family of superconductors with some common features that make them unique. They are layered compounds based on Cu-O planes lying normal to the c-axis and with critical temperatures around 100 K. Cu-O planes contain the mobile charge carriers responsible of the superconducting phenomena; carriers are sharply localized in these planes and, thus, cuprates are extremely anisotropic superconductors. All them are strongly type II superconductors ($\kappa=\lambda/\xi \geq\sqrt{2}$) with extremely short coherence length ξ and large penetration depth λ. Hence, their magnetic phase diagram is essentially dominated by the presence of vortices in a large variety of phases [122] (Fig. 1-16), which are the result of the

energetic balance between thermal energy, vortex-vortex interaction energy, pinning energy and coupling energy.

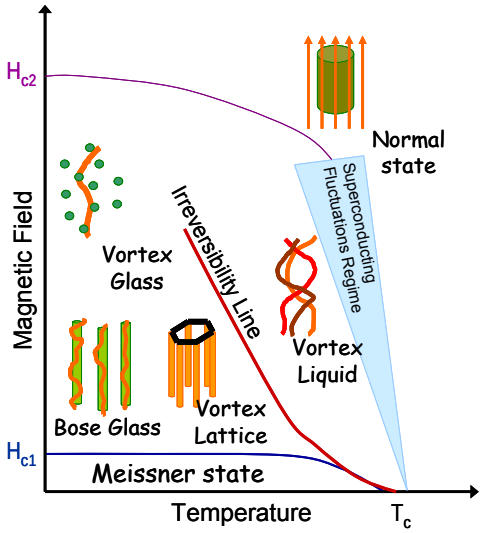

Fig. 1-16: Schematic representation of a magnetic phase diagram of a cuprate superconductor.

In defect-free crystals and at low temperatures, vortices are expected to arrange in an Abrikosov lattice. In presence and control of uncorrelated point defects such as oxygen vacancies or impurities, a solid state called vortex glass has been proposed which promotes the wandering movement of vortices [122, 123]. On the other hand, when the system is dominated by correlated linear or planar defects like dislocations or twin boundaries, the flux lines essentially localize in these defects. This phase is named Bose glass [124].

These solid phases are determined by the competition between vortex-vortex and vortex-defect interaction. The former favours the arrangement of vortices in a hexagonal lattice, whereas the latter promotes the appearance of a glass. At high temperatures, both energies are overwhelmed by thermal energy, which leads to the melting of the vortex solid state phase into a liquid phase. In crystals free of defects, transition from solid to liquid phase is of first order and it is called melting line [125]. In not so pure crystals, the dynamic response of the system shows a second order transition [126]. In this case, the line that separates the two regions is known as irreversibility line. In the liquid phase (H-T region above irreversibility line), flux lines move reversibly since they cannot be pinned. Despite the material is still in the superconducting state ($H<H_{c2}$) in the sense that order parameter $|\psi(r)|$ is not zero, the system is found in a resistive state. Hence, the technological applicability regime magnetic field – temperature of HTS is restricted below the irreversibility line, where defects present in the material act as effective vortex pinning centres. However, there exists an open debate about how

and how much the irreversibility line can be pushed towards upper critical field H_{c2}, which would enable to reach higher critical currents close to the depairing currents. An upper limit for the irreversibility line has been proposed [127].

The magnetic field-temperature diagram displayed in Fig. 1-17 shows the irreversibility line (solid lines) and upper critical field H_{c2} (dashed lines) of several superconductors [128]. It is observed that $YBa_2Cu_3O_{7-x}$ (YBCO) is the material displaying the highest irreversibility line at 77 K, which corresponds to the boiling point of nitrogen at atmospheric pressure. Use of nitrogen as refrigerant is commercially important because liquid nitrogen can be produced cheaply and it is not prone to some of the problems related to helium piping (solid air plugs, etc.). Hence, this behaviour justifies the choice of YBCO for the production of superconducting tapes even though it is not the material with highest critical temperature.

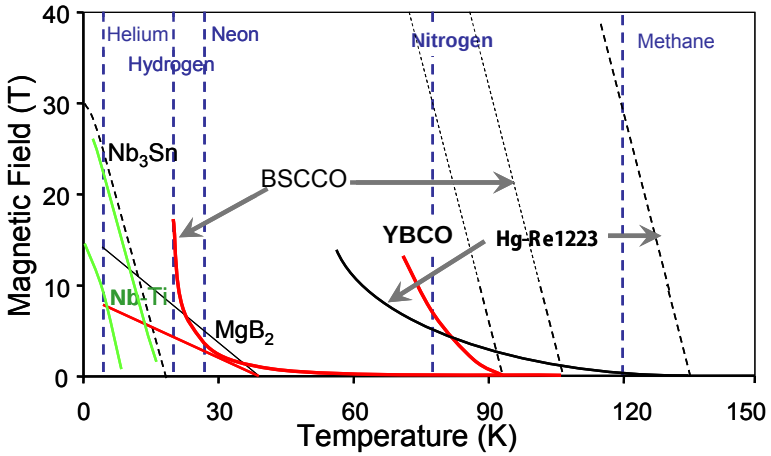

Fig. 1-17: Magnetic field-temperature diagram showing the irreversibility line (continuous lines) and the upper critical field H_{c2} (dashed lines) of several type II superconductors: Nb-Ti alloy, Nb_3Sn, MgB_2, $(Bi,Pb)_2Sr_2Ca_2Cu_3O_x$ (BSCCO) and $YBa_2Cu_3O_{7-x}$ (YBCO). At 77 K, YBCO presents the highest irreversibility line [128].

YBCO is a cuprate superconductor of high critical temperature, T_c= 92 K [119]. Its unit-cell, schematized in Fig. 1-18, is constituted by three perovskite blocks stacked vertically along crystallographic c-axis: one $YCuO_3$ perovskite with two adjacent $BaCuO_3$ perovskites, and some unoccupied oxygen positions. Each unit-cell has two Cu-O planes where the superconducting current flows. These planes are separated by charge-reservoir interleaved blocks which controls the carrier density in Cu-O planes. The oxygen sites in the Y plane are never occupied, whereas the oxygen positions on the third Cu-O plane (basal plane, situated in the reservoir blocks closing the cell) have average occupancies between 0 (x=1) and 0.5 (x=0).

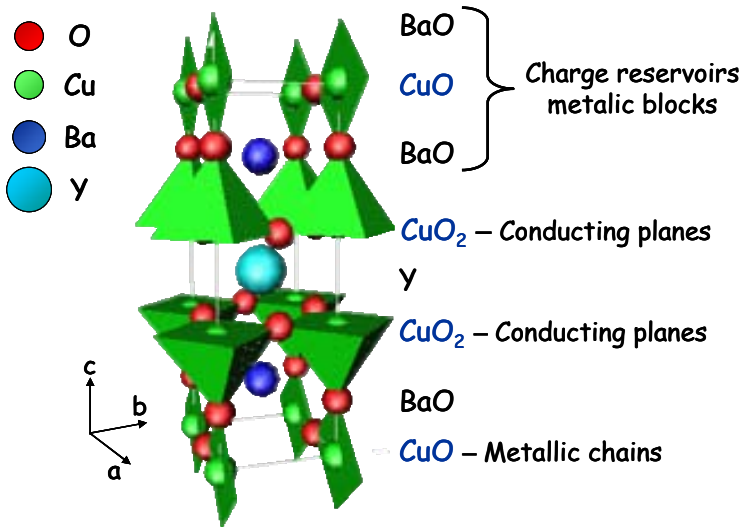

Fig. 1-18: Crystallographic structure of YBCO.

This compound can exist in two crystalline structures, tetragonal or orthorhombic, depending on the quantity and distribution of oxygens in the basal plane. For low oxygen concentrations ($x \geq 0.5$), oxygen atoms are randomly distributed over the four possible sites around cooper atoms in basal plane. It corresponds to the tetragonal phase, which presents an insulating behaviour. For x values close to 0, oxygen atoms order in chains with copper atoms along b-axis. This distribution corresponds to the orthorhombic phase, which is the superconducting phase. The maxim critical temperature is achieved for x~0.06; above x=0.06 the compound is overdoped and T_c drops. Fig. 1-19 shows the dependence of critical temperature of YBCO with x [129].

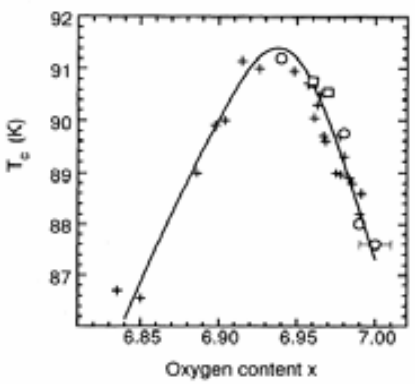

Fig. 1-19: Variation of T_c as function of oxygen content x in $YBa_2Cu_3O_{7-x}$ [129].

Due to its layered structure and strong localization of carriers in Cu-O planes, YBCO shows a high anisotropy like all HTS, i.e. its properties are very different along ab-planes or c-axis direction. Particularly, the current flowing parallel to Cu-O planes (ab-planes) is much higher than the current that can flow through the c-axis, $J_c^{ab} >> J_c^c$. A good alignment of ab-planes is essential for the easy flow of currents and to obtain high critical current densities.

Therefore, biaxial epitaxial texture is a critical issue that faces the preparation of YBCO thin films. The strong anisotropy of the material also influences the directional dependence of characteristic lengths ξ and λ. So, the flux line structure depends on the relative magnetic field orientation with respect to the crystallographic axes of the material. Table 1 summarizes ξ and λ dimensions of YBCO at T=0 K [119]; it must be noticed that both parameters vary with temperature as $(T_c\text{-}T)^{-0.5}$.

Table 1: Coherent length **ξ** and penetration depth **λ** of YBCO at T=0 K.

YBCO	λ (nm)	ξ (nm)
c-axis	890	0.24
ab-planes	135	1.6

The traditional way to phenomenologically describe YBCO is through Ginzburg-Landau theory [122]. Within the framework of this model, the material anisotropy is introduced through an anisotropic mass tensor, with components m_{ab} in the a-b plane and m_c in the c-axis direction. Consequently, the mass anisotropy ratio ε or the reciprocal parameter γ=1/ε is defined as

$$\gamma = \frac{1}{\varepsilon} = \sqrt{\frac{m_c}{m_{ab}}} = \frac{\lambda_c}{\lambda_{ab}} = \frac{\xi_{ab}}{\xi_c} \qquad \textbf{Eq. 1-14}$$

For YBCO, γ typical ranges between γ~5-8 [130]. This parameter is very useful to describe some properties of the superconductor. For example, the critical field or the critical current density can be scaled using parameter γ to that of an isotropic superconductor introducing the angular dependence factor ε(θ) like in [131]

$$\varepsilon(\theta) = \sqrt{\cos^2\theta + \frac{1}{\gamma^2}\sin^2\theta} \qquad \textbf{Eq. 1-15}$$

where θ is the angle between the magnetic field and the crystallographic c-axis. This approach is restricted to uniaxial anisotropy and to homogeneous anisotropic superconductors. Thus, it does not apply to physical properties that do not follow the intrinsic anisotropy of the material.

1.5.3 Nanostructuration of YBCO thin films: distinct approaches

The ability to transport currents without losses makes superconductors highly attractive for power applications [128]. Losses reduction that derives from the use of HTS materials leads to an increase of the efficiency in generation, transport and distribution of electrical energy at the same time that also diminishes the environmental impact.

Nowadays, YBCO tapes are considered the most promising material [132] among HTS for the development of applications in the electrical power area, such as magnets, cables, motors, power-transmission lines or fault current limiters. They constitute the so called "second-generation" superconductors or coated conductors, and they are essentially based on multilayers prepared by the epitaxial growth of superconducting coatings on thin film metal tapes. As clear advantages, YBCO shows low losses and carry high currents, and enables to work a 77 K where the use of nitrogen makes it much commercially available. At present, vacuum-based methodologies such as PLD allow the generation of YBCO superconducting tapes of high quality [132]. However, implementation in power applications falls on the development of low-cost fabrication routes to deposit large areas. Chemical solution deposition (CSD), which allows the growth of YBCO through an all-chemical path, has already shown a great potential to accomplish either low-cost and performance objectives [98, 133]

The capabilities of YBCO thin films to transport critical current densities 10-100 times higher than YBCO single-crystals is consequence of the large amount of defects inherent in film growth, such as oxygen vacancies, precipitates, dislocations or twin boundaries [132, 134]. However, these current-capabilities rapidly deteriorate when increasing temperature and magnetic field. So, once the basic difficulties associated to high quality films growth (avoid cracks, voids, high misoriented grains, etc.) have been surmounted, it is time to look for strategies to improve $J_c(H,T)$ performance. Typical YBCO critical current densities are far from depairing currents J_{dp}. The major challenge is, then, to know how much J_c can be pushed up.

Since naturally generated defects are the source for high J_c values of YBCO thin films, the most suitable strategy seems to consist of finding the way to nanoengineer materials in order to pin vortices under the desired H-T conditions. Choosing the appropriate type of defect to improve vortex pinning in the YBCO film is not straightforward. The pinning capabilities of a defect depends on its shape, size, composition, interaction with the superconducting matrix and with surrounding defects, etc.; and its performance also varies with temperature and applied magnetic field intensity and orientation. Optimization of pinning is achieved when the size of defects approaches the core radius (i.e. the coherence length ξ) and, thus, the best pinning defects for YBCO are those of nanometric size, since ξ~2-4 nm for YBCO at temperatures $\leq$ 77 K [130].

First approaches to nanostructure YBCO thin films were based on particle irradiation [135-137]. Particularly, heavy ion irradiation is a widely recognized approach to generate columnar defects [138]. However, this approximation is not scalable to commercial applications. Up-to-date, distinct routes to introduce impurities in the superconducting matrix are leading to outstanding results. One example consists of the insertion of impurities of the

non-superconducting phase of YBCO, Y_2BaCuO_5, by using alternate targets during PLD deposition [139]. Another nanocomposite alternative route widely investigated using PLD is based on the introduction of epitaxial nanoparticles of $BaZrO_3$ or $BaIrO_3$ through the preparation of mixed targets or through sequential deposition [140-143]. The outcome is the generation of random distributions of the mentioned particles or self-assembled nanostructures of BZO particles (Fig. 1-20) which result into a notorious enhancement of vortex pinning efficiency. In general, this improvement is due to dislocations generated at the interface as consequence of lattice mismatch between these oxide nanostructures and YBCO, or due to the structures formed by nanoparticles themselves, which produce correlated pinning enhancement. Outstanding results have been as well achieved though the growth of BZO particles within the YBCO matrix by CSD [144]. In this case, enhancement of isotropic pinning is achieved generating the largest isotropic pinning forces reported so far. Additionally, a low-cost all-chemical route easily scalable to large areas is used.

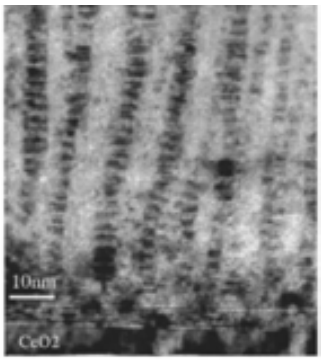

Fig. 1-20: TEM cross-section image showing the columnar structure of nanopillars of BZO within YBCO matrix; deposition was carried out by PLD [141].

A distinct approach to nanostructure YBCO thin films is based on surface decoration. It consists of the preparation of interfacial nanostructured templates prior to YBCO deposition, so that interfacial nanostructures are used to induce defects in the superconducting matrix grown above, which might act as effective pinning sites. Distinct examples of surface decoration based on vacuum deposition techniques have been reported, mainly inducing c-axis correlated defects [145]. Deposition of metals (Ag [115], Ir [146]) or oxide (Y_2O_3 [117, 145], CeO_2) nanoparticles on substrates, or induction of nanometric outgrowths in oxide thin films (CeO_2 [116], $SrTiO_3$ [147]) are the cases studied. Details of these results will be reviewed in chapter 7. Owing to the high potential of CSD to generate YBCO thin films, it would be interesting to prepare interfacial nanostructured oxide templates also by chemical solutions. The generation of interfacial nanostructured YBCO thin films prepared from an all-chemical approach might turn into a low-cost route to develop superconducting tapes, with pinning centres and superconducting properties similar or distinct to those of surface-decorated YBCO thin films grown by vacuum related methodologies. CSD-prepared nanocomposites with BZO

nanoparticles embedded in the YBCO matrix has already showed enhanced pinning mechanisms [144], but involving distinct kind of pinning sites than those obtained in vacuum-based techniques.

1.6 Thesis content

After this general introduction to the present knowledge about strain-induced nanoislands' formation, state-of-art of the generation of interfacial oxide nanostructures especially from chemical solutions and a brief summary of the phenomenon of superconductivity and current state of development, the rest of the thesis is structured as follows.

In chapter 2, we describe the main techniques used in the present work to characterize and analyze the samples prepared. Chapter 3 summarizes the experimental procedure followed for the preparation of the samples, which is based on chemical solutions. Heat treatment of substrates prior to deposition, precursor solution preparation and thermal treatments performed are described. It also comprises a brief summary of crystallographic structures used.

Chapter 4 shows the capabilities of CSD to prepare nanostructured templates of distinct oxide phases ($BaZrO_3$, $Ce_{1-x}Gd_xO_{2-y}$, La_2O_3). Influence of distinct growth parameters on the resulting interfacial nanoislands are studied in detail for each phase. Due to the particularities of interfacial $Ce_{1-x}Gd_xO_{2-y}$ nanoislands depending on the processing conditions, chapter 5 is entirely devoted to this kind of nanostructures. Accurate structural characterization is carried out. Specific experiments are performed to investigate the characteristics and behaviour of these nanostructures under different conditions. Chapter 6 also focuses on $Ce_{1-x}Gd_xO_{2-y}$ nanoislands but from a theoretical perspective. Calculations based on thermodynamic models are performed to determine their equilibrium shape. Kinetic mechanisms to explain their evolution are also proposed.

Finally, chapter 7 shows the application of prepared nanostructured templates in the field of high temperature superconductors. Interfacial oxide nanostructures are used as templates to improve the superconducting properties of YBCO thin films also grown from chemical solutions. Superconducting properties of these chemically-derived interfacial nanostructured YBCO films are analyzed in detail as function of temperature, magnetic field intensity and orientation and film thickness.

Chapter 2

Experimental techniques

Development and evolution of nanoscience and nanotechnology is strongly linked to the existence of techniques capable of characterizing the structural, chemical, physical, etc. properties of materials of nanometric dimensions. Through the present work, Atomic Force Microscope (AFM) has been the basic and essential tool to study interfacial nanostructured oxide templates. Knowledge and statistic data about basic morphology, size, density and distribution of interfacial nanoislands were continuously obtained from AFM topographic images. X-ray diffraction analyses based on a bidimensional detector (XRD^2) were regularly performed at ICMAB in collaboration with a specialized technician to determine the crystallographic orientation of the generated interfacial nanoislands. Reflection High-Energy Electron Diffraction (RHEED) measurements were done at Leibniz-Institut für Festkörper- und Werkstoffforschung (IFW) Dresden in collaboration with Dr. R. Hühne during my short stage.

Nanostructure and surface analyses were also carried out by Transmission Electron Microscope (TEM) and Field-Emission Scanning Electron Microscope (FESEM). SQUID-magnetometry and electrical transport measurements were used for the characterization of nanostructured superconductor $YBa_2Cu_3O_7$ (YBCO) thin films, and Focused-Ion Beam (FIB) was used for the localized milling of these superconducting thin films. Detailed studies of these complementary techniques were carried out by other members of the Superconductor Materials and Large Scale Nanostructuration group at ICMAB. Accordingly, just few details about these techniques are revised.

2.1 Surface characterization

2.1.1 Atomic Force Microscope (AFM)

Just two decades after its invention (1986) [148], AFM has become a decisive tool for the development and progress of nanoscience and nanotechnology. Acquirement of high

resolution 3D images in real space independently of the conductive properties of the sample and environmental conditions (gaseous, liquid or vacuum) are the main clues of its success. AFM performance is based on the detection of forces acting at nanometric scale between the atoms of a sharp mechanical tip (probe) and sample's surface. There exists a variety of forces, attractive and repulsive, whose relevance mainly depends on tip-surface distance. Short-range forces (D~1 nm) comprise repulsive forces due to Pauli repulsion or ionic repulsion, short-range forces of chemical bondings and capillarity forces. At larger distances (D ≥ 1 nm), long-range forces predominantly act, like Van der Waals forces between dipoles, and electrostatic and magnetic forces. The most important forces acting in AFM experiments are summarized in Fig. 2-1. Since the variety of detected tip-surface interactions not only restricts to atomic forces, the AFM is often more accurately called scanning force microscope (SFM).

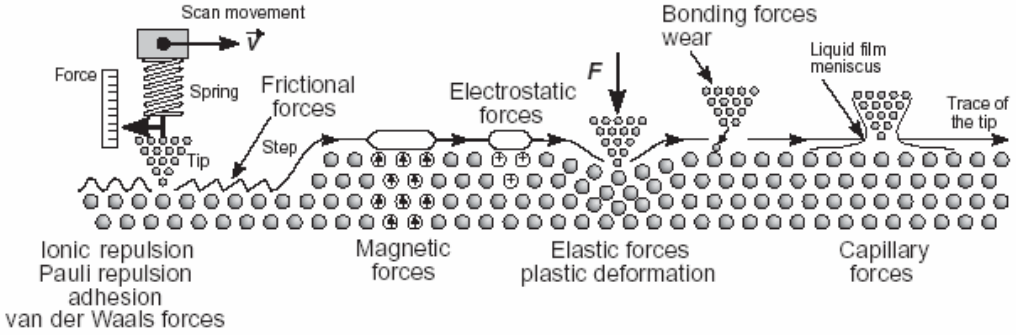

Fig. 2-1: Summary of the forces relevant in AFM [149].

The tip is mounted on a soft spring (cantilever); and surface-tip interactions are indirectly measured through deflection of cantilever. A scanner with piezoelectric components is used to move the tip and the sample relative to each other in all (x,y,z) directions. There exist different strategies to measure deflections; particularly, beam deflected technique is among most commonly used methods. As illustrated in Fig. 2-2, a four-quadrant photodiode detects a laser beam which is reflected on the back side of the cantilever. When the cantilever is not deflected, the reflected beam strikes the centre of the photodiode system. Any movement of the cantilever results into a displacement of the reflected beam from the central position and, consequently, one of the photodiodes receives more light than the others. A four-quadrant photodiode allows to quantify bending and torsion of the cantilever; so, it allows to measure both normal and friction forces between tip and sample's surface. Other methods to detect the deflection include the measurement of the sample-tip capacity or the measurement of the deformation of piezoelectric materials placed on the cantilever.

Variations of detected intensity are converted into electrical signal. Through feed-back systems, the electronics of the AFM acts on the dynamic response or the position of the

cantilever (depending on the work mode) to restore the reference set-point value. Changes of the control parameter are directly related to height variations at a given point of the surface. Scanning the whole x-y surface with the tip, topographic maps are obtained from the tip-surface interactions detected at each (x,y) point.

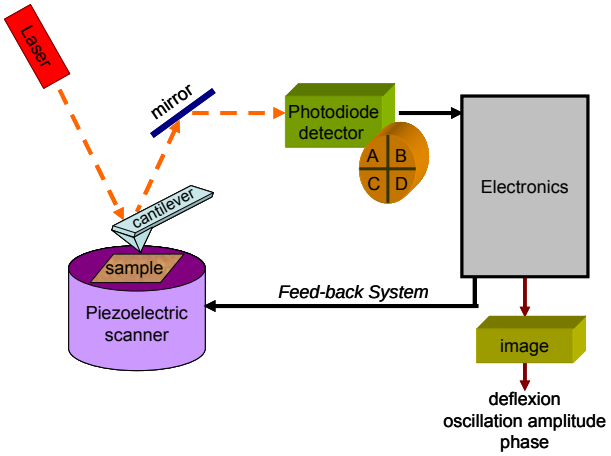

Fig. 2-2: Principle of operation of an AFM with laser beam deflection method.

Topographic AFM images contain quantified information in three (x,y,z) dimensions. Vertical resolution of 0.01 nm is typically achieved. However, piezoscans limitations do not normally allow to measure features higher than 10 μm relative to a flat surface. The maximum x-y scanning range with a typical piezoelectric is ~100 μm. The lateral resolution is mainly determined by the sharpness of the tip. Commercial tips have a typical curvature radius of ~10 nm. Fig. 2-3a shows a commercial Si tip attached to a cantilever. When scanning an object with dimensions close or inferior to probe's size, lateral sides of the tip will touch the feature before its apex and, thus, the electronics will start to answer to the elevation changes despite tip is still not interacting with the object. In these cases, the image reflects more the shape of the tip than the surface feature itself. This phenomenon is referred as tip convolution; it is schematized in Fig. 2-3b.

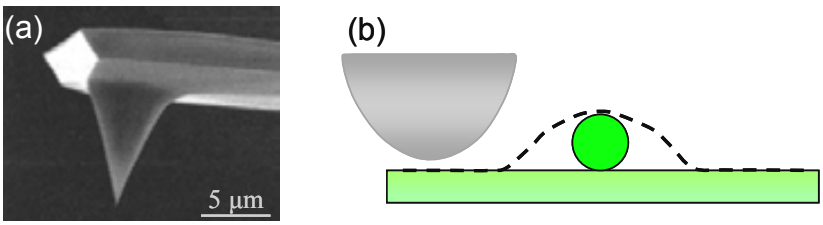

Fig. 2-3: Scanning electron microscope image of a commercial Si tip attached to a rectangular cantilever (a). Schematic representation of tip convolution effect (b).

The AFM can operate in a variety of modes mainly depending on the environmental conditions and purpose of the measure. A common classification of imaging modes is based on static (contact) mode and a number of dynamic (non-contact) modes. The former measures

cantilever deflection, whereas the latter measures dynamic properties of the cantilever such as (resonance) frequency, amplitude or phase.

- **Contact mode**: the tip is brought close to the surface, typically ≤ 5 Å. During initial contact, the last atoms of the tip feel a weak repulsive force due to the overlap of the electron orbitals with atoms of sample's surface, which causes the deflection of the cantilever. This movement is detected as mentioned above, and the equipment answers through the feed-back system changing the vertical position of the tip to keep deflexion at a reference value. Thus, the scan is performed at constant force. This mode can also operate at constant height.

Measurement of variations of repulsive forces with distance enables to obtain high resolution images. However, in ambient conditions surfaces are usually covered by a contaminant layer formed after the absorption of solid species and liquids, especially condensed water. When the tip touches this layer, a meniscus form and the cantilever is pulled towards the surface due to surface tensions. This phenomenon can cause damage of soft surfaces and distortions in the measurements. Thus, images obtained in contact mode are influenced by friction and adhesive forces. On the other hand, the tracking repulsive forces might be strong, resulting in wear of both the tip and sample's surface.

- **Non-contact mode**: in its version in dynamic mode, the tip oscillates close or at its frequency of resonance. The tip hovers 50-150 Å above the surface of the sample; thus, it mainly sense attractive Van der Waals forces. Because tip oscillates in a field of forces, the resonance frequency changes and the work frequency is distinct from the free oscillating frequency. Consequently, the quality factor Q related to damping also diminishes (high damping, small Q). In this mode, the cantilever is constantly oscillating close to the surface without touching it, and forces are detected measuring changes in amplitude, phase or frequency.

At the working region distance, attractive forces are considerably weaker than those detected in contact mode; so, resolution is generally lower. However, this mode is frequently used when dealing with soft samples or samples with lower adhesion to the substrate, since it causes minor damages to the surface.

- **Intermittent contact mode**: also known as tapping or a.c. mode, it arises as an excellent strategy to obtain high resolution images of sensible surfaces. The cantilever oscillates at constant frequency close to its resonance; and the tip is intermittently touching the surface of the sample. As a result, lateral forces as well as problems related to friction, adhesion, electrostatic forces or other difficulties are drastically reduced. The tip touches the surface during a very small period of its oscillation. So, if oscillating amplitude is sufficiently high, the

tip does not attach to the contaminant layer because the cantilever has enough restoring force to overcome it.

The amplitude of the oscillation is often used as the feed-back signal (amplitude modulation (AM) mode). When the tip scans a hill on the surface, the cantilever has less room to oscillate and the amplitude decreases. Contrary, if the prove passes over a depression in the surface, the amplitude increases towards the free oscillation amplitude. These variations in amplitude are used by the feed-back system to restore the feed-back set-point value, and enable to identify and quantify the topographic characteristics of the surface under study. The phase of the oscillation can also be used as feed-back signal. In tapping mode, the resolution is also influenced by the variation of quality factor Q due to damping. So, resolution is improved working in vacuum instead of environmental conditions.

The applications of SPM, as well as working fields, increase day after day. AFM is especially used to obtain topographic images of surfaces, insulating or conductive, in order to determine its roughness, grain size or other characteristics at micron and nanometric scale. Moreover, by studying other kinds of tip-sample interactions one can obtain information about other properties of sample's surface, such as electrical currents (*Electrical Force Microscopy*, EFM), magnetism (*Magnetic Force Microscopy*, MFM) or optics (*Near-field Scanning Optical Microscopy*, NSOM). The range of materials to investigate is also extensive, including semiconductors, biological samples, high resistive materials, etc. In addition to its use in research, SPM is also used by many companies to carry out routine quality controls.

Images presented in this work were done with a Cervantes AFM system from Nanotec Electronica and a PicoSPM of Molecular Imaging, both installed at ICMAB-CSIC. A microscope 5500 from Agilent Technologies located at Matgas-AIE was used when localization of a specific region of the sample was required, since it has an optical microscope and a micrometric positioning stage associated.

Images were taken in tapping mode and using silicon tips with characteristic resonance frequency of 150-200 Hz and stiffness constant of around 48 N/m. Surface was typically scanned by the tip at 1 lines/s. Three distinct kinds of data were captured:

- Topography: 3D images which provide information of features of the surface such as islands' size or distribution; z-data is encoded in a false colour scale, like in land topographic maps. Fig. 2-4a shows a topographic image of La_2O_3 nanoislands on $LaAlO_3$ (LAO) single-crystal substrate.

- Amplitude: these images are formed from the amplitude signal and arise as consequence of small changes of the oscillating amplitude due to the fact that feedback system cannot always respond instantaneously to the asperities of sample's surface. Amplitude images can be assumed as the error signal of the topographic images. The corresponding example is shown in Fig. 2-4b.
- Phase: it shows the phase difference between the oscillating signal sent to the cantilever to make it oscillate and the detected oscillation signal. Among other features, contrast obtained in this type of images (Fig. 2-4c) depends on material properties such as stiffness or viscosity.

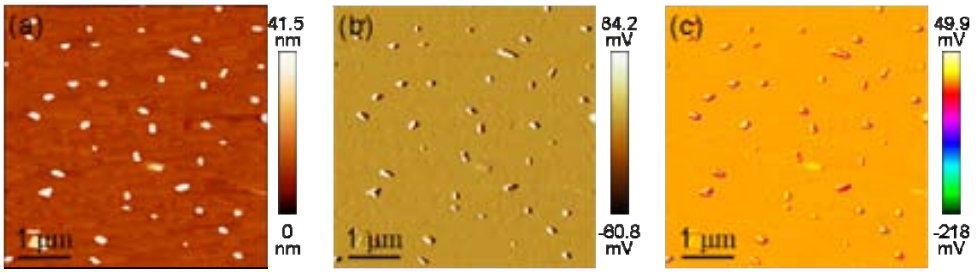

Fig. 2-4: 5x5 µm^2 AFM images taken in tapping mode of a nanostructured substrate with interfacial La_2O_3 nanoislands on LAO: topographic (a), amplitude (b) and phase (c) images.

Typical scans of 20x20 µm^2 were performed at distinct zones of the nanostructured template to study the homogeneity of islands' distribution. Scans between 5x5 µm^2 and 0.5x0.5µm^2 were done to study in detail the morphology, size and density of interfacial nanoislands. AFM images were processed with Mountains Map software from Digital Surf and WSxM from Nanotec Electronica. Previous to observation, samples were cleaned in acetone and methanol in an ultrasonic bath, and dried with compressed air. Then, they were exposed to ultraviolet light and ozone (UVO-Cleaner, Jetlight) for 30 minutes to eliminate the possible layer of gases absorbed on the surface, which might result into adhesion of the tip and diminution of resolution.

2.1.2 Reflection High-Energy Electron Diffraction (RHEED)

RHEED is a diffraction technique very sensitive to surface structure and morphology; particularly, its sensitivity to surface roughness is down to monolayer [150]. Thus, it is very suitable to characterize the structures of flat surfaces or to monitor the growth of thin films. In the present work, it was used to find out the crystallographic structure of interfacial nanoislands.

The RHEED system mainly consists of an electron gun which directs electrons towards a sample placed at the centre of a vacuum chamber. A small fraction of reflected electrons interfere constructively at specific angles and generate a diffraction pattern, which is captured on a CCD camera. The electron gun is one of the most important pieces since it limits the resolution of the system. It typically operates at 10-100 keV. The mean free path of electrons at

such energies is about hundreds of nanometers. Accordingly, surface sensitivity is achieved with incident grazing angles so that it is ensured that the beam remains close to the surface. Performance of measurements in vacuum chamber prevents scattering of electrons by gas molecules.

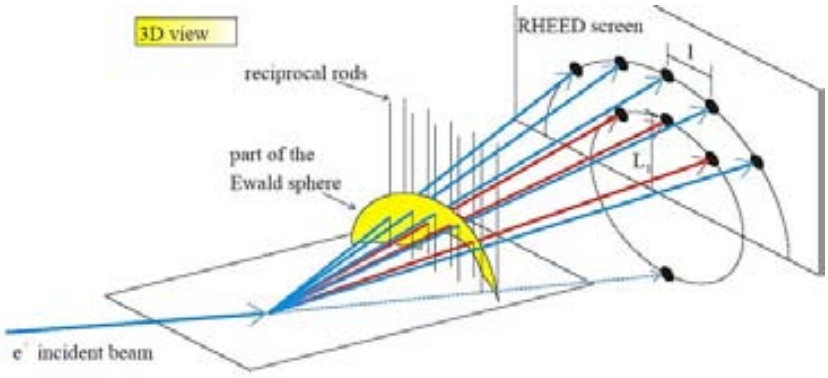

Fig. 2-5: Schematic 3D representation of elastically scattered electrons in real space.

The diffraction pattern at the detector is function of the surface of the sample. Patterns corresponding to perfect flat surfaces exhibit a collection of spots laying in concentric circles (Laue circles). Since only the first few layers of the material contribute to diffraction, the reciprocal lattice is a set of rods. Therefore, diffraction conditions for elastic scattering are satisfied when the rods of reciprocal pattern intersects the Ewald's sphere. Fig. 2-5 shows a 3D sketch of elastically scattered electrons in real space. However, most of the samples' surfaces are not ideal. Imperfections of the surface result in modifications of the shape of the diffracted beams, such as splitting or broadening of peaks.

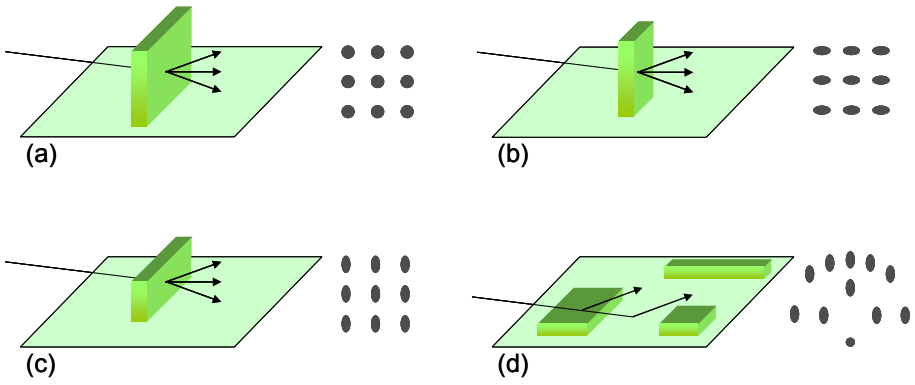

Fig. 2-6: Schematic illustration of distinct surface morphologies and corresponding RHEED diffraction patterns.

For rough surfaces, the high energy of electrons allows them to penetrate through the asperities and 3D islands of the surface. In this case, a transmission pattern is obtained, characterized by spots laying in straight lines (Fig. 2-6a). As the size of the crystal through which diffraction occurs gets smaller, the spots broaden in the direction in which size is reduced. Distinct possibilities of diffraction from 3D islands are shown in Fig. 2-6b and c.

Surfaces with flat terraces show a pattern combination of reflection and transmission electron diffraction (Fig. 2-6d). Amorphous surfaces give no diffraction pattern; in this case just a diffuse background would be obtained

RHEED measurements were obtained with a Staib Instruments system at IFW-Dresden using an electron beam of 30 kV, a beam current of about 50 μA and an incidence angle of less than 2° with respect to the substrate surface. The diffraction pattern was analyzed with a computer program based on the kinematics theory of electron scattering written by Dr. Sebastian Fähler (IFW Dresden).

2.1.3 Field Emission Scanning Electron Microscope (FESEM)

Conventional SEM provides topographical and elemental information at magnifications of 10x up to 100000x. This kind of microscope is very suitable to obtain surface information about grain size, porosity, particle's distribution or material inhomogeneities, for example. Besides material evaluations, it is also used for failure analysis or quality control screening. Since the sample is investigated with electrons, it must conduct electricity. Observation of bad conducting or insulating samples can be achieved through coating with a thin conductor layer such as gold. However, coating avoid, as well as improvement of resolution, can be nowadays achieved by using a Field-Emission SEM (FESEM). In this case, electrons are accelerated under the influence of a strong electrical voltage gradient (field) which enables to generate narrow proving beams with low or high electroenergy. As a result, spatial resolution is improved (up to 10 nm) and sample charging and damage is minimized.

The rest of the principle of operation of a FESEM is mainly the same of a SEM. A beam of electrons (primary electrons) is focused on a sample placed in a vacuum chamber. As a result of this bombardment, electrons from the specimen are dislodged (secondary electrons). Removed electrons are attracted and collected by a positively charged detector and translated into signal. To obtain a (FE)SEM image, the electron beam sweeps back and forth across the surface of the sample. Secondary electrons imaging provides information about surface features. The gathered information is 2D, no quantized information in z-direction is obtained. Asides from secondary electrons, the primary electron beam also generates backscattered electrons and characteristic X-ray, which can also be detected and analyzed.

FESEM images were made using a FEI QUANTA 200 (FEG-ESEM) located at ICMAB. Insulating oxide nanoislands of less than 50 nm lateral size on insulating $LaAlO_3$ substrates could be imaged without coating working at 3-20 kV in high vacuum. Surface

characterization of superconducting thin films was carried out with a JOEL JSM-6300 SEM in the "Servei de Microscopia Electrònica" at "Universitat Autònoma de Barcelona" (UAB)

.

2.1.4 Focused Ion Beam (FIB)

FIB uses a beam of gallium ions (Ga^+) to image the surface of a sample in a way similar as the electron beam in a SEM. Unlike electrons, when the primary beam of gallium ions hits the surface of the sample it sputters neutral atoms or secondary ions; and it also produces secondary electrons. The primary Ga^+ beam is rastered over the surface to study, and the sputtered ions or secondary electrons are collected to form an image of the surface.

As higher is the primary beam current, more material is sputtered from the surface. Hence, low primary beam currents are used for imaging, whereas high-beam operation is used to sputter or remove material from the surface, such as during high-precision milling or cross-sectioning of a specific area. It must be noticed that gallium atoms can be implanted in the outmost layers of the specimen, which might damage the sample.

Sputtering capacity of FIB was used in the present work to diminish the thickness of patterned bridges in nanostructured YBCO thin films. A dual beam FIB Zeiss 1560XB located at "Centre Nacional de Microelectrònica" (CNM) was used. The milling was done in layers at 30kV/200pA; so, different thickness' reductions were achieved with different milling times. At the end of the milling, the resulting surface was cleaned by milling at very low current conditions (30kV/50pA) to remove possible Ga^+ ions implanted at the surface of YBCO thin film. A FESEM incorporated in the same system allowed the simultaneous visualization of the sample with electrons without damaging it.

2.2 Structural characterization

2.2.1 X-Ray Diffraction (XRD) analyses

X-rays are a powerful tool to explore the atomic arrangement of a wide range of materials, since X-ray wave length is comparable to the distance of atoms in a crystal (~Å). When an X-ray beam is directed towards a sample, some photons primarily collide with electrons in atoms and are diffracted in all directions. Elastically scattered waves can interfere constructively. If the atoms within the sample are arranged in a periodic fashion, the diffracted wave will reflected the symmetry of the atoms' distribution.

In accordance with Bragg law, the condition that must be fulfilled to obtain constructive interaction between beams diffracted by parallel planes of atoms is

$$2\,d_{hkl}\sin\theta = n\,\lambda \qquad \textbf{Eq. 2-1}$$

where d_{hkl} is the spacing between *hkl* planes, θ the angle and λ the wavelength of the incoming X-ray beam and n an integer number.

Modifying the incidence angle θ, one obtains a diffraction pattern which is characteristic for each crystalline specimen, since it contains information about positioning of atoms in the material. Diffraction pattern is indexed by comparing it with an international data base in order to identify the crystalline specimen. Each material gives always the same diffraction pattern. Hence, in a mixture of materials each one produces a diffraction pattern independent of the others. Relative rotation of the sample with respect to the detector enables to explore diffraction in distinct configurations and get information about preferred alignment of crystallites (2θ-scan), their out-of-plane (ω-scan) or in-plane (Φ-scan) texture, etc. Fig. 2-7 displays a schema of the nomenclature of angles that can be typically adjust in a XRD measurement.

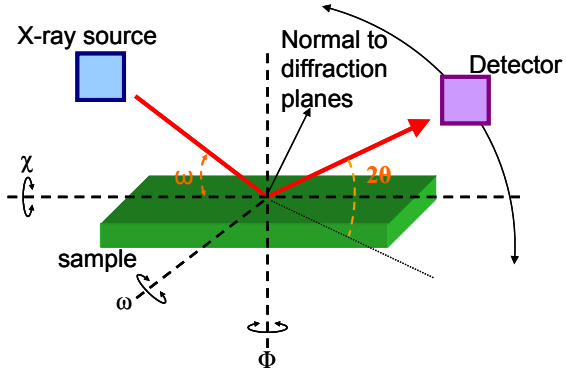

Fig. 2-7: Schematic view of the nomenclature of angles that can be adjusted in XRD measurements.

Therefore, XRD is a versatile and non-destructive technique commonly used to characterize, for example, thin films. In the present work, 2θ-scans were performed to obtain information about the preferential crystallographic orientation and possible existence of secondary phases in oxide thin films. These measurements were performed at ICMAB using Siemens D5000 and a Rigaku Rotaflex RU-200BV diffractometers with Cu-K_α λ=1.5418 Å.

2.2.1.1 Two-dimensional X-Ray Diffraction (XRD^2)

Conventional X-ray measurements are confined within a plane. Thus, various additional samples rotations are required to gather information about diffraction patterns out of this plane. This is a typical example of the problems avoided using a two-dimensional X-ray detector

(XRD^2). These detectors enable to capture diffraction patterns in 2D directions, i.e. diffractions measurements are not longer confined within the diffraction plane [151].

There exists a large variety of XRD^2 configurations to carry out a large variety of applications. A typical XRD^2 system consists at least of a 2D-detector, X-ray source, sample alignment, sample positioning stage, monitoring device and corresponding electronic and computer systems to visualize, store and treat the diffraction data. As a result, the geometry of the XRD^2 is based on three geometry spaces: diffraction space, detector space and sample space.

For a bidimensional flat detector, the detector surface can be considered as a plane which intersects the diffracted rays, like it is sketched in Fig. 2-8a. For a single-crystal, the diffracted beam points to discrete directions, which are imaged as points in the ideal case. For a polycrystalline sample, the diffraction pattern is formed by diffraction cones. Depending on the position of the detector, the conic sections might be circles, ellipses, parabolas or hyperbolas, as illustrated in Fig. 2-8b. Each 2D image acquired in a single exposition is called frame (Fig. 2-10a), and it contains information over the selected range of 2θ and χ values.

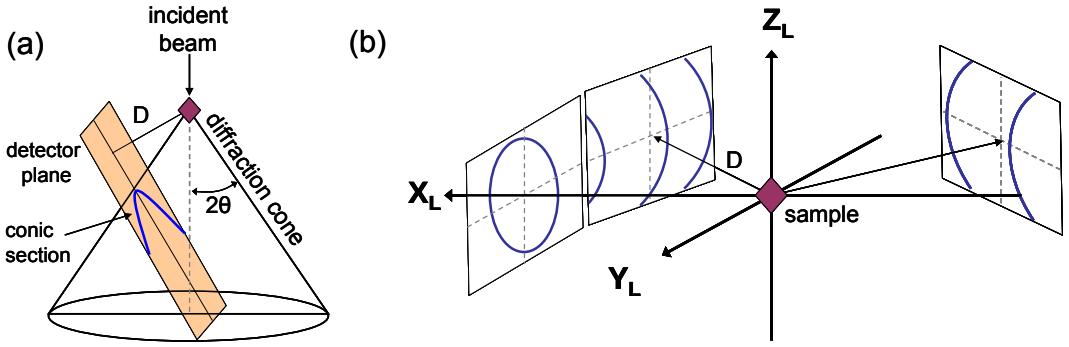

Fig. 2-8: Diffraction cone and conic section of a with a 2D plane detector (a); detector position in the laboratory system X_L, Y_L and Z_L, where D is the sample-to-detector distance [151].

Diffraction profiles equivalent to those acquired from XRD punctual detector can also be obtained from 2D diffraction patterns integrating in χ over a selected 2θ range. Then, the identification of data is carried out with the same procedure that in conventional diffractometers. Nevertheless, data integrated from XRD^2 patterns exhibits better intensity and statistics to carry out phase identification and quantitative analysis in textured samples.

XRD^2 is also highly interesting to perform texture analysis [152]. These studies base on the fundamental relationship between the pole figure angles and the distribution of intensities along a diffraction ring. Since numerous diffraction rings are simultaneously measured, also are the pole figures. To obtain a one-dimensional pole figure, all data points on a diffraction ring are considered.

Moreover, XRD^2 also enables to perform measurements of stress in a fast, high sensitive and precise way.

The XRD^2-based studies presented in this work were done using a GADDS D8 Advance system from Bruker at ICMAB. Since different χ values are simultaneously detected in a single exposure (2θ-χ frame), XRD^2 was very suitable to simultaneously analyze the polycrystalline and epitaxial part in a film. For example, Fig. 2-9 displays a XRD^2 diffraction pattern of a YBCO thin film grown by chemical methods at ICMAB. The spots indicate the epitaxial growth of the film, whereas the diffraction rings point out that there is also part of the volume randomly oriented. The possibility to detect in one 2θ-χ frame the same reflection corresponding to distinct crystallographic domains present in the sample (under the appropriate diffraction conditions) was very useful to quantify the volume fraction of each domain. This procedure will be used in chapter 7 to determine the epitaxial fraction of YBCO film oriented (00ℓ) and (ℓ00) or (0ℓ0).

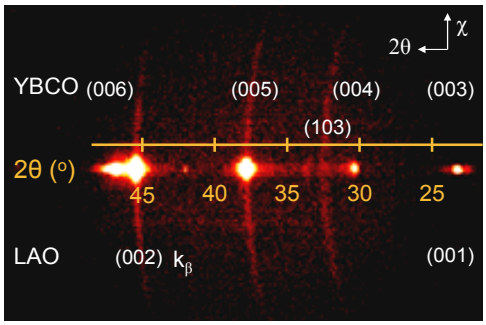

Fig. 2-9: XRD^2 diffraction pattern of a YBCO thin film. The diffraction rings indicate that part of the film is randomly oriented.

Nonetheless, what really made this technique crucial throughout the present work was the possibility to routinely determine the crystallographic orientation of interfacial oxide nanostructures. Conventional X-ray measurements are not suitable to resolve nanometric structures since the signal from our interfacial nanoislands was completely disguised by that coming from LAO substrate due to the small amount of deposited material (less than one nanometre equivalent thickness) in front of 0.5 mm thick single-crystal. A specific practice was established to carry out crystallographic orientation identification of our nanoislands by XRD^2. At selected 2θ-χ regions, ϕ-scans (in-plane rotation around the centre of the sample) were done in 180 steps of 2°; each position was held for 40 seconds to get enough signal. As a result 180 2θ-χ frames like the one displayed in Fig. 2-10a were obtained.

Integration over a determined 2θ range enables to construct the ϕ-scan; because we represent it in polar coordinates we often refer to it as pole figure. The χ position of the diffraction peaks indicates the angle between the chosen reflection and the planes parallel to substrate's surface. Therefore, the crystallographic orientation of interfacial nanostructures

could be determined. Obviously, any crystallographic orientation present in just small volume of the sample was not detected. Fig. 2-10b displays a typical ϕ-scan obtained for a template with interfacial CeO_2 nanoislands. The (111)-CeO_2 peak was chosen because it corresponds to the reflection of highest intensity. From the position of these peaks (i.e. angle χ between (111)-CeO_2 planes and those CeO_2-planes parallel to the interface), CeO_2 dominant crystallographic orientation is determined. Complete pole figures should be required to investigate all χ range, however, after initial studies we just focused on χ-values of our interest accordingly to the analysed samples.

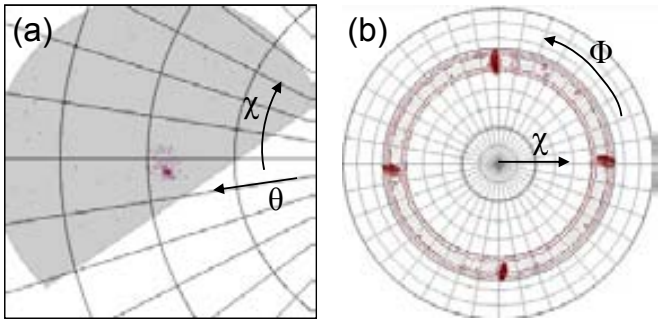

Fig. 2-10: XRD[2] frame centred at $2\theta=28.5^o$ and $\chi=54^o$ of a nanostructured template with CeO_2 nanoislands (a); the peak observed at $2\theta=28.5^o$ corresponds to (111)-CeO_2 reflection. ϕ-scan (*pole figure*) constructed after the integration between $27^o<2\theta<29^o$ of the 180 frames measured (b); peaks at $\chi=54^o$ indicate that the investigated CeO_2 nanoislands are (001)-oriented.

2.2.2 Transmission Electron Microscope (TEM)

TEM comprises a range of powerful techniques aimed to obtain internal structural information (arrangement of atoms, defects, etc.) of a material using different imaging and diffraction techniques, and also to get compositional information about elements and compounds constituting a sample.

TEM operates on similar basic principles to those of an optic microscope, where electrons are used instead of light. A highly coherent beam of electrons is directed towards a sample which is specially prepared to thickness (<200 nm) so that electrons can transmit through it. Ideally, the transmitted electron intensity distribution is magnified and focused by a system of electromagnetic lens into either an image or a diffraction pattern. The image can be digitalized and recorded by a CCD camera system. The contrast in a TEM image depends on the specific TEM technique and conditions we are using. For example, for conventional bright field images, the darker areas of the image correspond to those regions of the sample where fewer electrons were transmitted through (i.e. thicker or denser).

Low magnification TEM images and electron diffraction patterns were acquired with a 200 KV Jeol JEM-2011 microscope at UAB and a 300 KV Philips CM30 microscope at

"Serveis Cientifico-Tècnics" of the Univeristat de Barcelona (UB). High resolution TEM images were performed using a Jeol 2010 FEG electron microscope operated at 200 KV at the "Serveis Cientifico-Tècnics" of the UB. Ultra-high resolution TEM images were taken with a 200 KV Cs-corrected F20-SACTEM Tecnai microscope at CEMES (Toulouse). Samples were cut to look at the island (or film)/substrate interface from side view (cross-section) or to look at the sample from the direction perpendicular to the island/substrate interface (planar view). Samples were prepared by using the mechanical tripod polisher technique followed by Ar milling [153]. Direct electron images provided information about shape, size, lateral facets, interface, etc. of interfacial oxide nanoislands. Electron diffraction patterns were used to identify the crystallographic structure of the nanoislands. Reconstruction of a TEM image (IFFT) with specific spots of the Fast Fourier Transform (FFT) enabled to study specific details of the nanostructures such as dislocations or Moiré fringes.

2.3 Superconducting properties

2.3.1 Inductive measurements: SQUID magnetometer

SQUID (Superconducting Quantum Interference Device) magnetometers are instruments with high sensitivity to measure in a non-invasive way the magnetic moment of a sample, from which the magnetization and magnetic susceptibility can be obtained. The versatility of these systems permits to perform both dc and ac measurements of magnetic moments. In the present work, dc-magnetometry was used to investigate the electromagnetic response of superconducting YBCO thin films.

SQUID magnetometer consists of a SQUID-detection system and a precise temperature control. The detection system is based on a set of pick-up coils located at the centre of a superconducting coil which can provide high magnetic fields. The sample is placed inside the superconducting coil so that it is submitted to uniform magnetic fields applied parallel to its c-axis. During the measurement, the sample is moved along the pick-up coils. As a result, a current proportional to the magnetic flux variation is induced in them. This signal is amplified by a SQUID sensor, which acts as a highly sensitive current-voltage converter detecting voltage variations proportional to sample's magnetization. This sensor can resolve magnetic moments of the order of 10^{-9} A·m^2 (10^{-6} emu). The whole system is placed inside a helium cryostat, which enables to refrigerate the superconducting coil and carry measurements between 5 K and room temperature.

Inductive measurements were carried out at ICMAB using two SQUID magnetometers from Quantum Design provided by 5 T and 7 T superconducting coils, respectively. To ensure good homogeneity of magnetic field and temperature during measurements, displacements of

the sample within the coils were not larger than 2 cm. Fig. 2-11 exhibits a typical measurement of the magnetic moment as function of the applied magnetic field H||c of a 275 nm thick YBCO thin film grown on a 5x5 mm^2 nanostructured template. To perform these measurements, the sample was cooled down to 5 K at zero magnetic field. Then, the magnetic moment was measured as the field was increased up to a certain field $\mu_o H_M$ (lower branch) and reduced down to 0 T (upper branch).

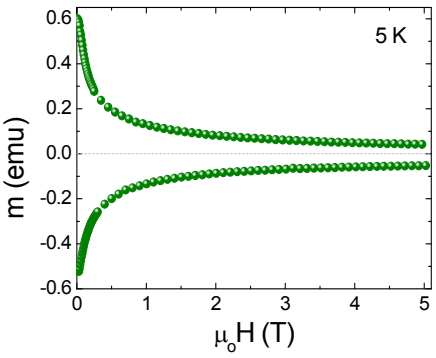

Fig. 2-11: Inductive SQUID measurement of magnetic moment as function of applied magnetic field at 5 K of a superconducting YBCO-TFA thin film grown on an interfacial nanostructured template.

From magnetization measurements, the critical current density of the superconducting film was determined through the Bean model [154, 155]. For a thin film with disk shape [156], the critical current density J_c can be calculated through the equation

$$J_c = 30\frac{\Delta m}{2\pi R^3 t} \qquad \textbf{Eq. 2-2}$$

where R is the radius of the disk, t the thickness of the film and Δm the width of the saturated hysteretic circle (i.e. when the superconductor is fully penetrated and the internal field is considered similar to the applied field). Dependence $J_c(H)$ is obtained from the dependence of the magnetization with magnetic field, M(H).

2.3.2 Electrical transport measurements

Critical current densities can also be determined from electrical transport measurements. Ideally, the critical current (I_c) is defined as the maximum current that can flow in a superconductor without dissipation. When the applied current exceeds I_c, the resistance become non-zero and a drop in voltage is measured. So, critical current densities can be determined from I-V curve, more generally from J-E curves.

Electrical transport measurements were carried out with a Physical Properties Measurement System (PPMS) from Quantum Design at ICMAB. The system essentially consists of a 9 T superconducting magnet and a helium cryostat. Precise control of temperature

within the range 1.8 - 400 K can be achieved. The system also has a nanovoltimeter and a dc/ac current source which can provide currents from 1 μA to 2 A with a resolution of 0.1 μA.

The sample was mounted in a single-axis rotor with a total angular range of 370° with a precision of 0.1°. So, the dependence of critical current densities with temperature and magnetic field intensity and orientation, $J_c(\theta, H, T)$ could be investigated. Prior to measurements, silver contact pads were deposited by thermal evaporation at 10^{-6} mbar on YBCO thin films and then annealed under oxygen atmosphere at 400°C for 1 h to ensure good electrical contacts with resistances below 10 μΩ. Afterwards, patterns with bridges of ~20 μm width and ~0.1-1mm long in four point configuration were done by photolithography [157].

In four point configuration, a dc-current was ramped till a desired value I_M between two pads and the voltage was read between two other pads. These I-V curves were obtained for distinct magnetic fields and temperatures. In the present work, the current required to develop an electric field of 1 μV/cm inside the superconductor was the criterion used to determine I_c (J_c). Fig. 2-12 displays a typical J-E curve at 77 K and self-field of an interfacial nanostructured YBCO thin film.

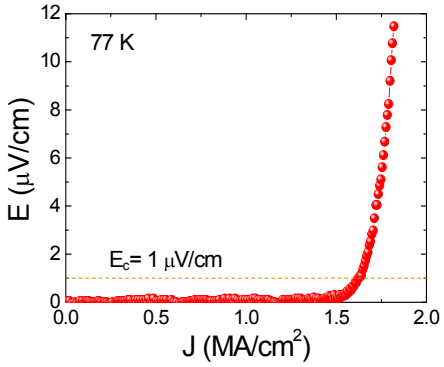

Fig. 2-12: Typical current-electrical field J-E curve of an interfacial nanostructured YBCO-TFA thin film at 77 K and self-field showing a critical current density of 1.6 MA/cm^2.